

# JGR Solid Earth

## RESEARCH ARTICLE

10.1029/2022JB024131

### Key Points:

- We investigate magnetostratigraphy and cyclostratigraphy of Chinese Loess Plateau aeolian sediments since the late Miocene
- The strong imprint of 1.2 Myr obliquity was responsible for the global climate transition during ~7 Ma cooling and 5.3 Ma warming
- The 1.2 Myr obliquity and 405 Kyr eccentricity modulations played key roles in the paleoclimate before and after 4 Ma, respectively

### Supporting Information:

Supporting Information may be found in the online version of this article.

### Correspondence to:

R. Zhang and V. A. Kravchinsky,  
ruizhang@nwu.edu.cn;  
vadim@ualberta.ca

### Citation:

Qin, J., Zhang, R., Kravchinsky, V. A., Valet, J.-P., Sagnotti, L., Li, J., et al. (2022). 1.2 Myr band of Earth-Mars obliquity modulation on the evolution of cold late Miocene to warm early Pliocene climate. *Journal of Geophysical Research: Solid Earth*, 127, e2022JB024131. <https://doi.org/10.1029/2022JB024131>

Received 29 JAN 2022

Accepted 31 MAR 2022

### Author Contributions:

**Conceptualization:** Jie Qin, Rui Zhang, Vadim A. Kravchinsky  
**Formal analysis:** Vadim A. Kravchinsky, Taslima Anwar  
**Funding acquisition:** Rui Zhang  
**Investigation:** Jie Qin, Rui Zhang, Vadim A. Kravchinsky, Jianxing Li, Yong Xu, Leping Yue  
**Methodology:** Jie Qin, Rui Zhang, Jianxing Li, Taslima Anwar  
**Project Administration:** Rui Zhang  
**Resources:** Rui Zhang  
**Software:** Taslima Anwar  
**Supervision:** Rui Zhang, Vadim A. Kravchinsky  
**Validation:** Jie Qin, Rui Zhang, Vadim A. Kravchinsky, Jianxing Li, Taslima Anwar

© 2022. American Geophysical Union.  
All Rights Reserved.

## 1.2 Myr Band of Earth-Mars Obliquity Modulation on the Evolution of Cold Late Miocene to Warm Early Pliocene Climate

Jie Qin<sup>1,2</sup> , Rui Zhang<sup>1,2</sup> , Vadim A. Kravchinsky<sup>1,2</sup> , Jean-Pierre Valet<sup>1,3</sup> , Leonardo Sagnotti<sup>4</sup> , Jianxing Li<sup>5</sup>, Yong Xu<sup>6</sup> , Taslima Anwar<sup>1,2</sup>, and Leping Yue<sup>1</sup>

<sup>1</sup>Department of Geology, Institute of Cenozoic Geology and Environment, State Key Laboratory of Continental Dynamics, Northwest University, Xi'an, China, <sup>2</sup>Geophysics, Department of Physics, University of Alberta, Edmonton, AB, Canada, <sup>3</sup>Institut de Physique du Globe de Paris, Paris, France, <sup>4</sup>Istituto Nazionale di Geofisica e Vulcanologia, Roma, Italy, <sup>5</sup>Chengdu Center of Geological Survey, Geological Survey of China, Chengdu, China, <sup>6</sup>Xi'an Center of Geological Survey, China Geological Survey, Xi'an, China

**Abstract** The climatic transitions during the Miocene-Pliocene epochs had significant impacts on the worldwide biological diversity and were associated with large turnovers of continental vegetation and fauna. Previous studies have shown that late Miocene cooling and continental aridification which was initiated 7 Ma reversed to warm conditions across the Miocene-Pliocene Boundary ~5.3 Ma. Here, we present detailed orbital pacing of Asian monsoon deposits to constrain further the global climate change during this period. We produce high-resolution magnetic susceptibility records which reveal that the 1.2 Myr obliquity modulation would have been the main driving factor of the cooling and warming that occurred ~7 and 5.3 Ma, respectively. The Tibetan rise and closures of the Panama and Indonesian seaways enhanced the impact of the 405 Kyr eccentricity cycles to an oscillatory climatic state while the Northern Hemisphere glaciations were increasing from 4 to 2.5 Ma.

**Plain Language Summary** For the first time, we point out eolian sediments from Chinese Loess Plateau through the Asian monsoon is primarily respond to the long-period evolving dynamics of Earth-Mars obliquity modulation since the late Miocene. Our study deciphers the presence of oscillatory sedimentary patterns resulting from the 1.2 Myr band were responsible for the global climate transition during the aridification and cooling at ~7 Ma and warming at ~5.3 Ma. Our new discovery challenges the previous hypothesis that carbon circulations involving both the marine and terrestrial carbon reservoirs were instrumental in driving late Miocene climate cooling and warming, which provide a valuable analog for the climate prediction of Pliocene-like temperature level in the coming decades.

## 1. Introduction

In the late Miocene, terrestrial environments and ecosystems have undergone tremendous changes due to the presumed decline of atmospheric CO<sub>2</sub> between 8 and 6 Ma (Beerling and Royer, 2011; Bolton & Stoll, 2013). This period has seen the replacement of large areas of tropical and subtropical forests by deserts (such as Sahara Deserts) and the expansion of C4 grassland (Cerling et al., 1997; Huang et al., 2007; Schuster et al., 2006). The large restructuring of vegetation and landscape coincided with major turnovers in animal communities (Badgley et al., 2008). However, those continental environmental upheavals do not bring direct information on the temperature change during the late Miocene (Herbert et al., 2016). The marine isotope record younger than the middle Miocene is characterized by periodic anomalies of the Antarctic ice volume that have been shown to be probably driven by obliquity in marine sequences from the peri-Antarctic margin (Naish et al., 2009). No clear trend suggests a long-term climatic change during the late Miocene (Lewis et al., 2008; Westerhold et al., 2020; Zachos et al., 2001). Recently, the integration of marine sea-surface temperature (SST) made it possible to estimate the evolution of global temperature during the Miocene (Herbert et al., 2016; LaRiviere et al., 2012). The late Miocene cooling did not lead monotonically to the ice age in the northern hemisphere that prevailed through most of the Pliocene (LaRiviere et al., 2012). Furthermore, temperature proxies indicate that cooling (Dowsett et al., 2005; Fedorov et al., 2006; Ravelo et al., 2004) and aridification (Lawrence et al., 2006) ceased during the Pliocene and that warmer conditions occurred after 5.3 Ma. Because the present-day global warming may induce

**Writing – original draft:** Jie Qin, Rui Zhang, Vadim A. Kravchinsky  
**Writing – review & editing:** Jean-Pierre Valet, Leonardo Sagnotti, Taslima Anwar

Pliocene-like temperatures during the next decades, a good knowledge of the transition from a cold late-Miocene and warm early middle Pliocene climate may provide a valuable analog for climatic projections (Burke et al., 2018).

It remains uncertain whether there is a link between contemporaneous atmospheric circulation, ecosystem changes in continental environments and the orbital variation effects recorded by climate proxies from the ocean realm. The hundreds of thousand-years time scale low-latitude processes such as monsoon forcing on the upper-ocean circulation and its productivity strongly influence climate dynamics and constrain the reconstruction of ice volume and atmospheric greenhouse gas concentrations (Holbourn et al., 2018). The high topography of the Tibetan-Pamir Plateau contributes to amplifying the Asian monsoon system that controls precipitation as well as the level of convection (An et al., 2001; Boos & Kuang, 2010). During the Quaternary, the climate was mostly affected by variability of precessional insolation modulated by the 405 and 100 Kyr eccentricity cycles and the 41 Kyr obliquity band (Hao et al., 2012; Nie, 2018; Nie et al., 2008; Y. Sun et al., 2019). In earlier records from the late Miocene to Pliocene, some may show unconventional cycles related to the orbital inclination rates of Earth and Saturn, called 173 Kyr metronome for Asian monsoon, which arouses our interest (Zhang et al., 2022). From the analysis of the obliquity solution, both the 173 Kyr and 1.2 Myr obliquity bands are of particular importance, the signal from the second is even stronger than that of the first one (Laskar, 2020). In order to detect the longer orbitally forced cycle that has not been studied in the monsoon region, and to estimate whether it is associated with critical late Miocene-Pliocene climate transitions, we choose the eolian red clay deposits as the research subject.

## 2. Material and Methods

### 2.1. Material

The monsoonal system is primarily characterized by intense summer rainfall over a wide area that lies along the continental-ocean pressure gradient and brings rainfall onto the continent (An et al., 2001; Y. Sun et al., 2019). The East Asian monsoon controls the amounts of precipitation and dust brought from the Indian Ocean to the Pacific Ocean by seasonal changes of warm moist air. Dry winds from the Asian high latitudes transported dust that yielded the formation of the Chinese Loess Plateau (CLP; Hao et al., 2012; Figure 1a). The Liulin (LL) eolian red clay section (N37°21', E110°45') is flanked to the east by the Lüliang Mountains and to the west by the Yellow River, dozens of kilometers away from the large mountain ridges (Figure 1b). The 68 m thick wind-blown deposits consist of brownish-red clay with sporadic and smaller caliche nodules (<5 cm) and abundant Fe-Mn coatings at the top intercalated by carbonate horizons. The bottom of the wind-blown deposits in the LL section was dated late Miocene by comparing the *Hipparion* teeth discovered at 56.3 m in the LL section with the analogous fossil layers in the neighboring Wujiamao and Fuxing sections (Xu et al., 2013; Zhang et al., 2022). This constraint enabled us to establish a first chronology of the LL section after correlating the magnetostratigraphic data to the geomagnetic polarity timescale (GPTS; Ogg, 2012).

### 2.2. Methods

#### 2.2.1. Sampling and Laboratory Measurements

Thirty samples at 2 m stratigraphic spacing were selected for thermomagnetic analyses using an MFK2 Kappabridge with a CS-4 furnace under an argon atmosphere to prevent oxidation during heating. Oriented paleomagnetic samples ~ every 10 cm and cut into 2 cm thick cubes for paleomagnetic measurements. A total of 618 samples were measured at 20 cm, increased to 10 cm in the parts where polarity reversals were more frequent. The samples were stepwise demagnetized every 50°C from room temperature up to 600°C using an MMTD 80 thermal demagnetizer. The natural remanent magnetization was measured using either a spinner JR6-A magnetometer or a 2G-755 magnetometer located in a low magnetic field space (<100 nT). The directions of the characteristic remanent magnetization were estimated by principal component analysis (Krischvink, 1980). Only determinations with maximum angular deviation below 10° were accepted.

The magnetic susceptibility (MS) of powdered samples was measured using a Bartington MS-2 susceptibility meter. Grain size (GS) analysis was performed with a Mastersizer 2000 laser particle analyzer. 0.2 g powder

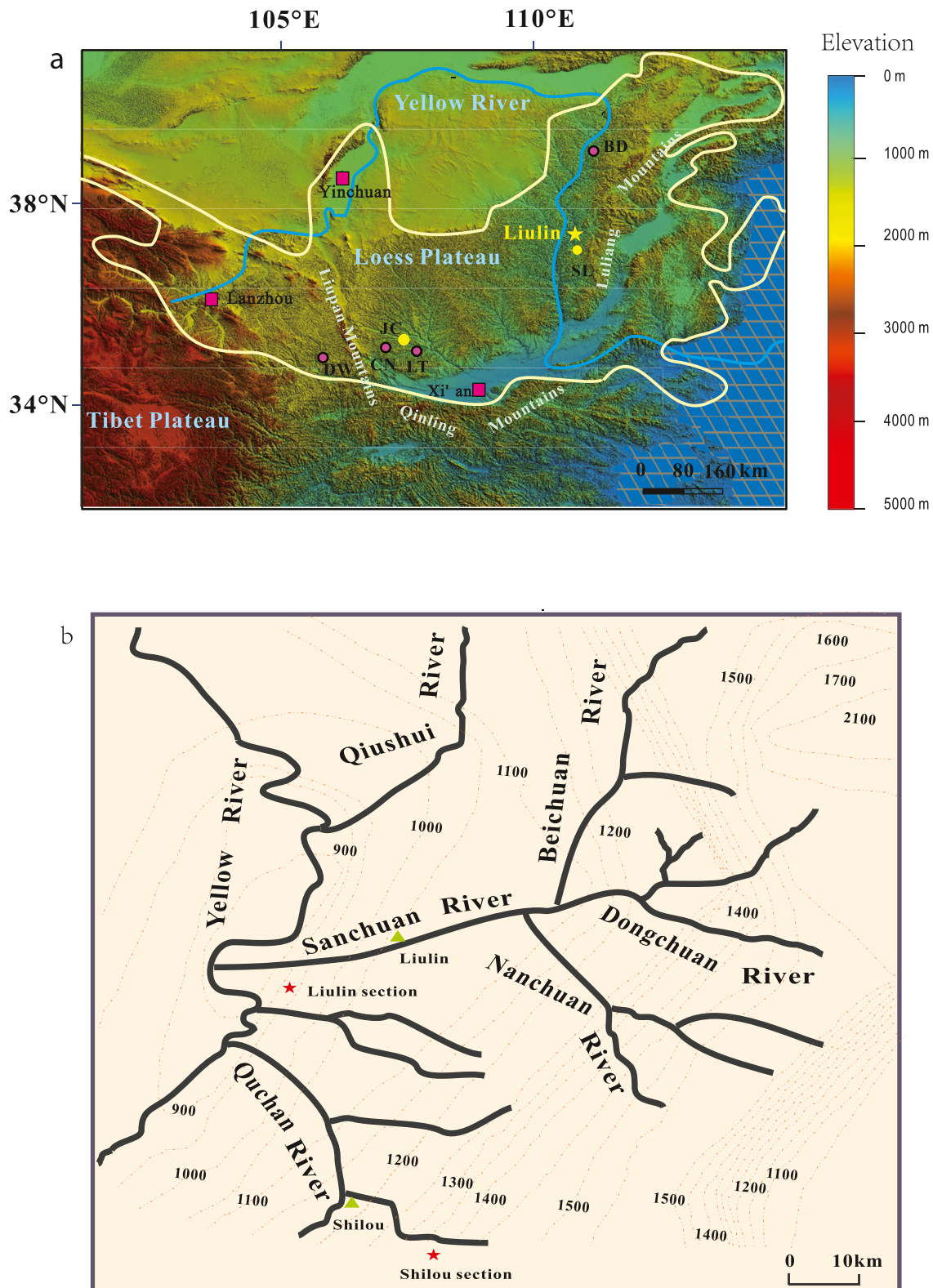


**Figure 1.** (a) Topographic map of the present-day Chinese Loess Plateau with studied locations (yellow star and yellow dots). Liulin (yellow star); SL, Shilou, JC, Jingchuan. (b) Map showing the location of LL (green triangle) and SL (red star) red clay sections and the surrounding main rivers. Red dashed lines represent the contours and the elevation is in meters.

samples were first treated with 10%  $\text{H}_2\text{O}_2$  for about 15 min to remove organic matter and to ensure that the excess peroxide was destroyed. Carbonate was removed using a 10% boiling HCl solution of 10 ml and the samples were dispersed for 15 min with 10 ml 10%  $\text{Na}(\text{PO}_3)_6$  in an ultrasonic bath prior to the measurements. We performed a cyclostratigraphy analysis through spectral analysis of the MS and GS stratigraphic trends. We repeated the procedure to generate several new correlations between the magnetic polarity zones and the GPTS till the orbital periods were resolved clearly in the MS and GS stratigraphic trends.

### 2.2.2. Spectral Analysis

Spectral analysis was applied to check the occurrence of Milankovitch periodicities in MS and GS trends by attempting several correlations between each magnetic polarity pattern and the GPTS (Anwar et al., 2015; Zhang, Kravchinsky, Qin, Goguitchaichvili, & Li, 2021; Zhang, Wei, et al., 2021). Wavelet analysis with 95% confidence level of background red noise was used to calculate the spectra of the MS and GS records (Torrence & Compo, 1998). Before spectral analysis, we removed the long-term trends by subtracting a fitted smooth line in order to minimize the effects of non-orbital periods. We established initial magnetostratigraphy and then generated several correlation patterns between each magnetic polarity pattern and the GPTS until the best orbital bands were clearly observed. After confirming the magnetochronology, both 405 and 100 Kyr cycles were extracted by filtering bands at the same time (with two bandwidths of 350–500 and 80–125 Kyr separately) in Matlab. Coherence between the band-pass filtered MS and eccentricity was scrutinized by calculating a correlation coefficient between the two-time series at zero phase using Matlab codes throughout the late Miocene—early and middle Pliocene. We shifted the MS curve toward younger or older ages by  $\sim 30$ –200 Kyr steps that were imposed by the coherency analysis in order to maximize the coherency between the two-time series with a zero-time lag; then, a new time series could be obtained from the tuning process. The process was repeated many times until each peak of the two curves matched well and the correlation coefficient at zero-time lag reached the maximum. Midway in the process, for a very small time lag between the two series, we stretched or squeezed the MS curve manually to make it match the eccentricity. Each tuned timescale was also applied to GS records at the same time. The spectral powers were produced to help determine our final age model.

## 3. Results

### 3.1. Rock Magnetism and Magnetostratigraphy

The plots of MS ( $\chi$ ) vs. temperature ( $T$ ) show that the heating and cooling cycles are nearly reversible (Figure 2). The sharp drop of  $\chi$  between  $\sim 400^\circ\text{C}$  and  $585^\circ\text{C}$ , indicates the presence of magnetite. Further decrease of  $\chi$  to  $700^\circ\text{C}$  reveals that hematite is also present. Representative demagnetization results for different depths are shown in Figure 3 with orthogonal vector diagrams. Our demagnetization results demonstrated that the low-temperature overprints generally ranged from room temperature to  $200^\circ\text{C}$ . After the elimination of the low-temperature component, the samples yielded a stable characteristic remanent magnetization (ChRM) tending to the origin.

Paleomagnetic analysis reveals five normal (N1–N5) and five reversed (R1–R5) polarity intervals from the reliable ChRM directions (Figure 4). All magnetostratigraphic intervals are established based on more than 4 coinciding samples (and over at least 0.8 m in the depth) to exclude the effects from small amplitude and short period anomalies (Zhang et al., 2018; Zhang, Kravchinsky, et al., 2021; Zhang et al., 2022; Zhang, Wei, et al., 2021). Three brief normal polarity events (less than or equal to 4 coinciding samples and less than 0.8 m in thickness) were also verified from the ChRM recording (red horizons in Figure 3). Sand, gravel and mammalian fossils found in the lower part of the section show negligible significant influence from alluvial processes (Figure 4a). The dense carbonate layers and mudstone indicate that the rainwater during the uplift of the Lüliang Mountains was not only in the form of surface flow but could also enrich the groundwater horizons. Groundwater is capable of reducing the iron oxides causing substantial re-magnetization of the eolian sediments. We marked five prominent layers, that could be affected by the groundwater, with light green shading in Figure 4.

The fossils found from sandy layers at 56.3 m in the depth of the section containing the *Hipparion* fauna were dated between 7.2 and 6.8 Ma at the adjacent Fuxing section, 7.0–6.7 Ma at the Wujiamao and Baode sections (Xu et al., 2013; Zhang et al., 2022; Zhu et al., 2008). Here, *Hipparion* teeth are thought to be  $\sim 6.8$  Ma in the



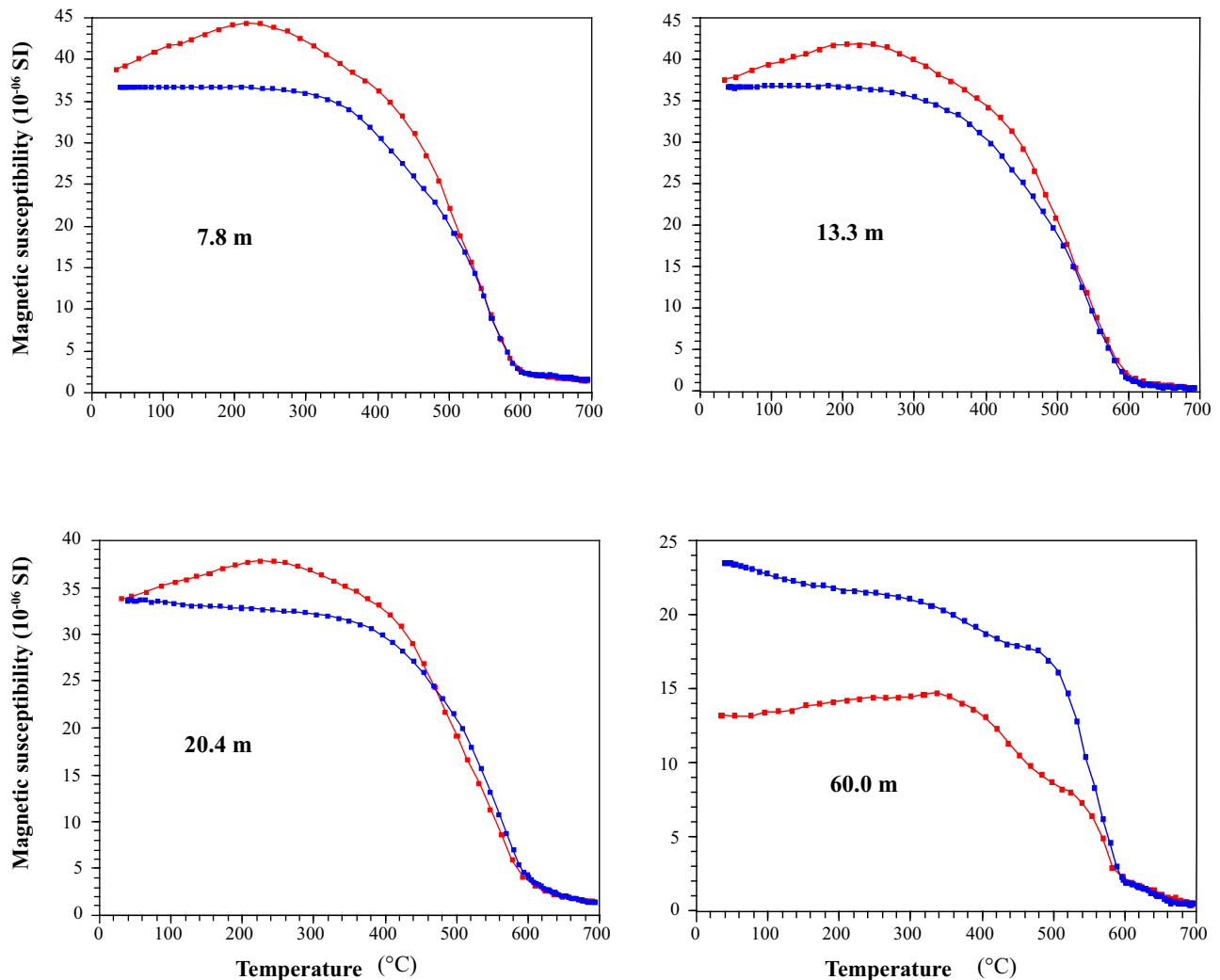


**Figure 2.**  $\chi$ - $T$  curves for selected samples from the Liulin red clay sequence. The red and blue lines represent heating and cooling curves, respectively.

magnetostratigraphy when N5 and R5 are correlated to C3An and C3Br. This constraint enabled us to establish the first chronology after correlating the magnetostratigraphic data to the geomagnetic polarity timescale (GPTS; Ogg, 2012). Following the visual correlation, N1–N3 are associated with C3n.1n–C3n.3n while a brief normal event remains a question mark with respect to C3n.4n. In the field observation, dense calcareous nodules, mudstone, and carbonate layers developed from 18 to 27 m, which means underneath the short polarity record at ~18 m, records of rising groundwater flows had been continuously superimposed in the stratum from 27 m and above. Such rework could have disrupted the original ChRM, causing the remagnetization to obscure the previous record. The lower two events at ~60 m from the section are only recorded in the sandy layer. As paleomagnetic samples in the sand are likely acquired viscous magnetic fields through remagnetization, further verification of the authenticity is required for these question marked red horizons (Zhang et al., 2018; Zhang, Kravchinsky, et al., 2021; Zhang et al., 2022; Zhang, Wei, et al., 2021). Considering dense carbonate and sandy layers developed at the depth of 41–46 m, it indicates that groundwater might also affect the remnant magnetization of the N4 polarity zone. In this case, only N1, N2, N3, and N5 can be used for the initial targeting age prior to tuning to the orbital parameters. Then, we performed a cyclostratigraphy analysis through spectral analysis of the MS and GS records. To verify the correctness of our magnetostratigraphic correlation we generated several new correlations between the magnetic polarity zones and the GPTS and performed spectral analysis until the orbital periods were clearly resolved in the MS and GS records. Clear peaks of the 405 Kyr eccentricity band can be observed between 7 and 5.4 Ma (Figures 5a and 5c). The 100 Kyr cycles can also be identified at around

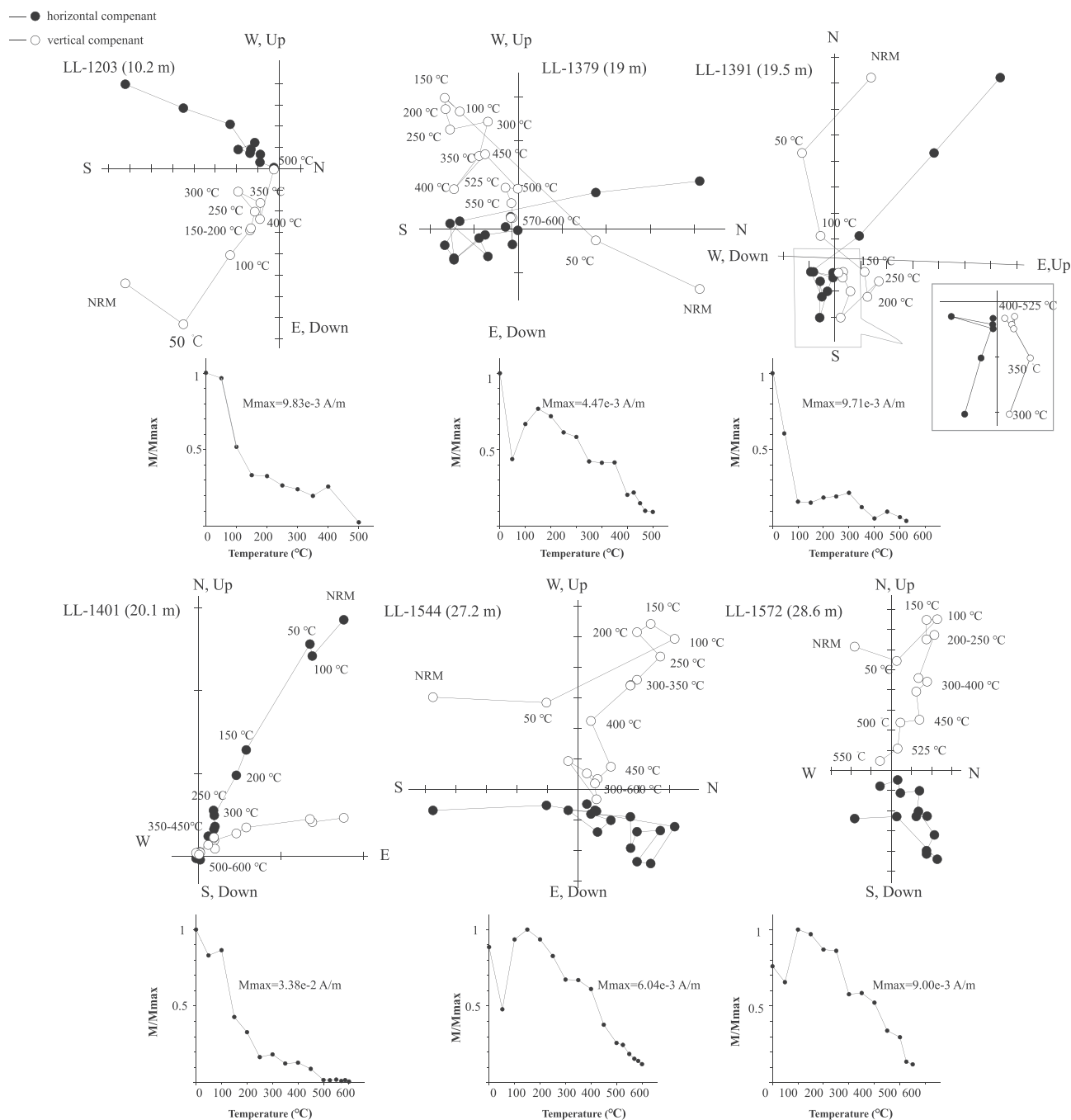


**Figure 3.** Representative thermal demagnetization curves for different depths.

6.2–6 Ma in the MS spectrum even though their power amplitudes were much weaker than the 405 Kyr power (Figure 5a). Analogously, a relatively low-amplitude 100 Kyr cycle revealed between 5.9 and 5.7 Ma in the GS spectrum (Figure 5c). The final magnetostratigraphic correlation that incorporated the cyclostratigraphic procedure described in Methods is shown in Figure 4.

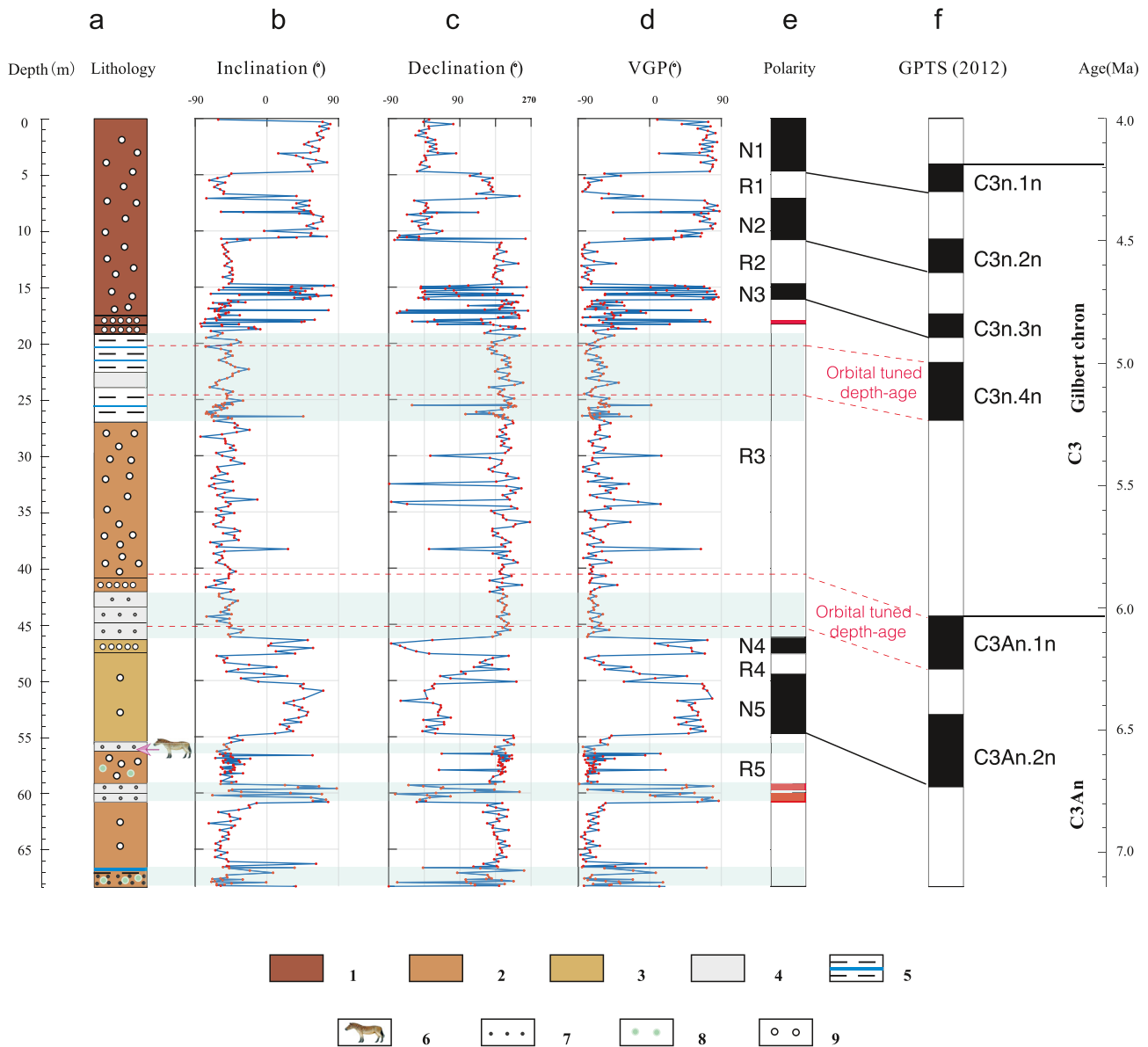


**Figure 4.** Lithostratigraphy, inclination, declination, and VGP as a function of depth, and the magnetic polarity interpretation of the Liulin red clay section, together with a correlation to the geomagnetic timescale (Ogg, 2012). Red dots show the measuring samples. Legend: 1—red clay with strong pedogenesis, 2—sandy red clay, 3—red clay with weak pedogenesis, 4—carbonate layer, 5—mudstone, 6—fossil, 7—sandstone, 8—gravel, 9—carbonate nodules.

### 3.2. Orbital Tuning and Astronomical Calibration

Once the magnetostratigraphic age of the LL section has been compatible with the cyclostratigraphy, we conducted two-channel-band filtering (405 and 100 Kyr) for both MS and GS data to highlight the visibility of the eccentricity band and tunes the filtered record cycle-by-cycle to the long eccentricity maxima (405 Kyr) and short eccentricity maxima (100 Kyr) at the same time (Figure 5). To examine the coupling between our records and eccentricity cycles, we calculated the correlation coefficient between filtered MS and eccentricity at zero phases. Then we shifted the filtered MS curve to the left or right at a short time span implied by the coherency analysis in order to fit it with the filtered eccentricity 405 Kyr until the correlation coefficient was maximized. After that, we carried out fine adjustments to the stronger 100 Kyr cycle improving further the correlation coefficient. We repeated this procedure until the curve matching and correlation coefficients were maximized. During the tuning processes, we also adjusted some small-time lags between the two series, by stretching or squeezing

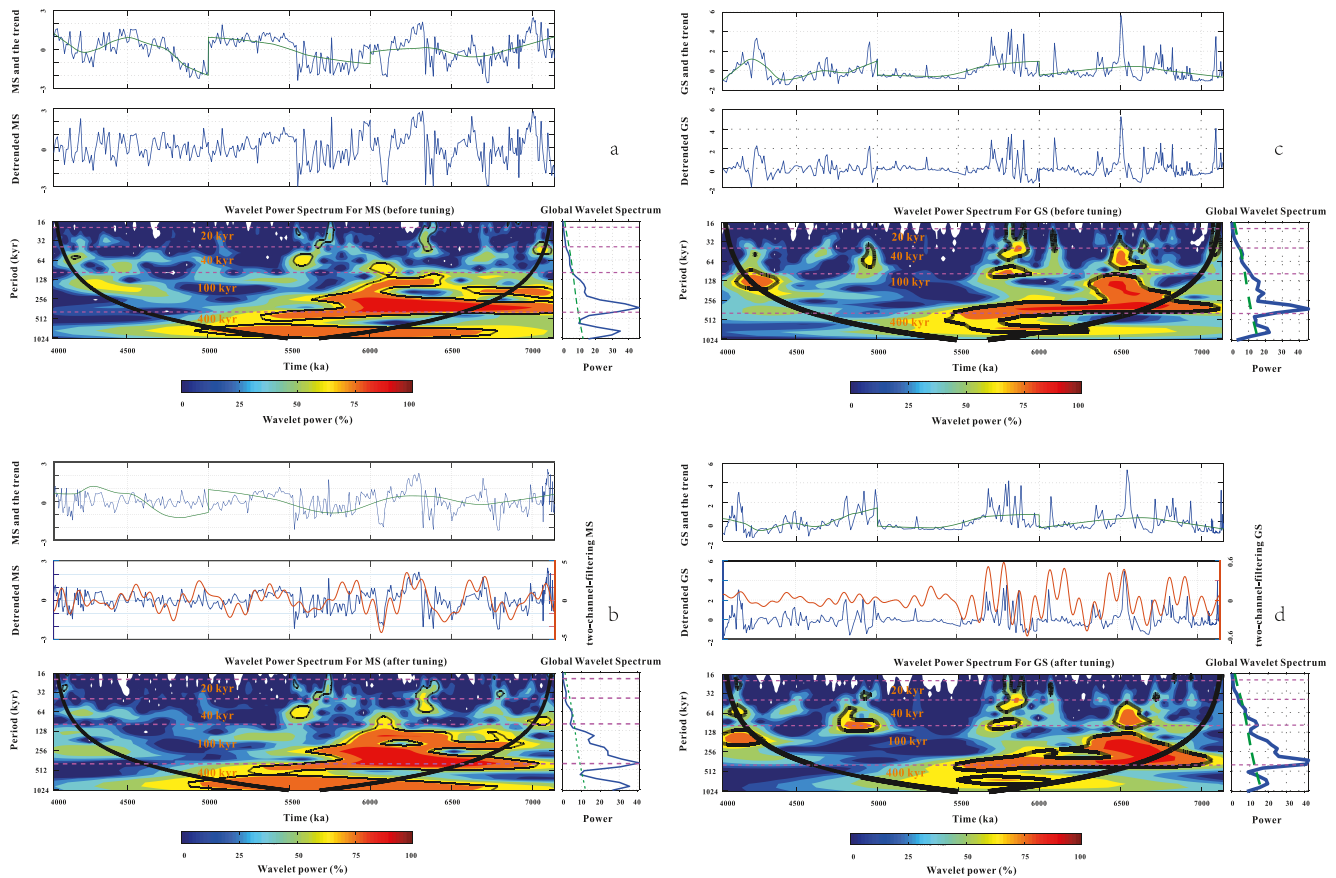


**Figure 5.** Wavelet analysis of the magnetic susceptibility signal before (a) and after tuning (b), the coarse fraction ( $>63 \mu\text{m}$ ) content before (c), and after tuning (d). Magnetic susceptibility (MS) and grain size (GS) was detrended with the Lowess smoothing method. The red line is the two-band-filter signal with bandwidths of 350–500 and 80–125 Kyr. The green solid line shows the long trend of MS (a, b) and GS (c, d) signals. The purple dashed line marks the orbital period. The thin black contour encloses regions of greater than 95% confidence for a red-noise process with a lag coefficient of 0.8. The thick black contour indicates the cone of influence. The global wavelet spectrum to the right illustrates the mean red noise spectrum, as indicated by the green dashed line. The color bars correspond to wavelet power.

the MS peaks to the eccentricity peaks (Figure 5b). The final astronomical calibration based on the MS turning was applied to the GS record (Figure 5d).

The calculated sedimentation rate (Figure 6) varied from 1.6 to 3.6 cm/Kyr with an average of 2.2 cm/Kyr. These values are typical of the eolian red clay dust in the CLP (e.g., Anwar et al., 2015; Nie et al., 2008; Zhang et al., 2018).

### 3.3. Stratigraphic Correlations

To investigate large-scale climate variations we first compare the LL section to the classical Jingchuan section (JC) which is located in the middle of CLP (Ding et al., 2001), and the adjacent Shilou (SL) section which is situated close to LL and stratigraphically continues LL to the younger age until 2.6 Ma (Anwar et al., 2015; Ding et al., 2001; Figure 7). Further comparisons to the eastern and western edges of CLP can be found in Figure S1 in Supporting Information S1.

The bottom age of the SL section was extensively debated and assigned from the late Miocene at 11 Ma (Xu et al., 2009, 2012), 8 Ma (Ao et al., 2016, 2018), to the early Pliocene at 5.2 Ma (Anwar et al., 2015; Zhang et al., 2018, 2022). Both Ao et al. (2016, 2018) and Xu et al. (2012) mistakenly assigned the finding of micromammal *Meriones* sp. at a depth of 46.6 m in the SL section to correspond to the Miocene age. However, the original studies of Zheng and Zhang (2000, 2001) cited by Ao et al. (2016, 2018) did not confirm that the *Meriones* sp. belonged to the Miocene. Zheng and Zhang (2000, 2001) established that another micromammal *Pseudomeriones*



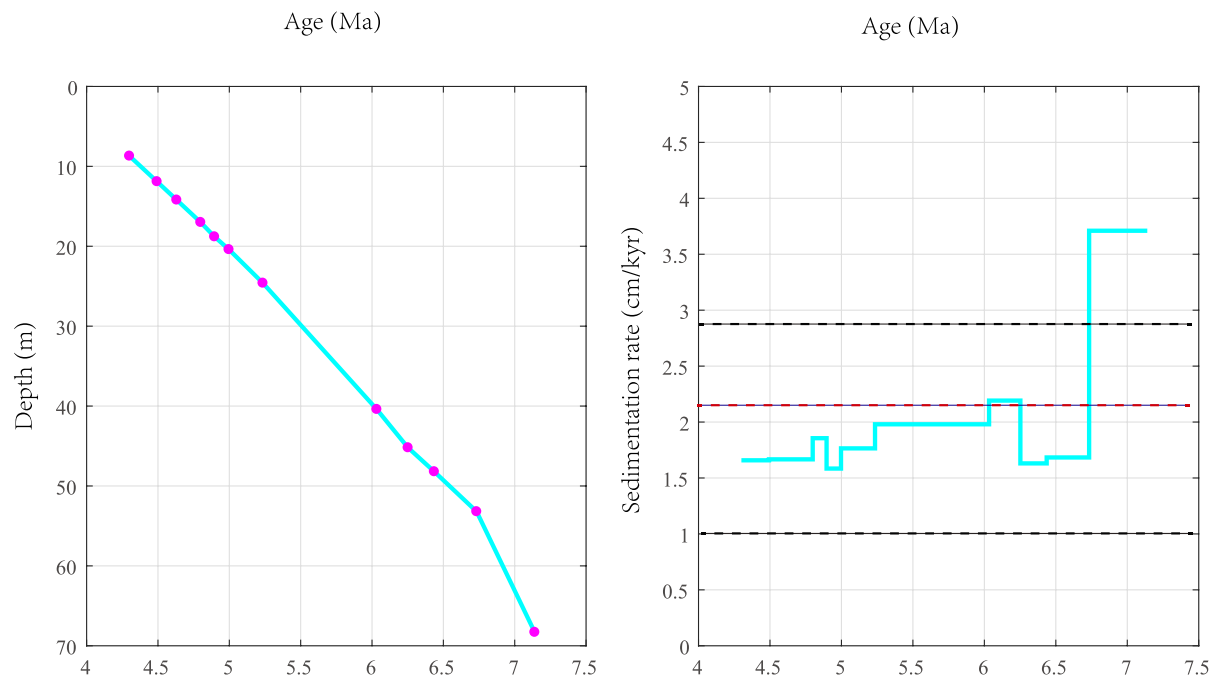


**Figure 6.** Sedimentation rates are determined on the basis of the magnetostratigraphic correlations. Black dashed lines denote the typical sedimentation rate range for the red clay of the Chinese Loess Plateau (CLP; Zhang et al., 2018). The red dashed line represents the average sedimentation rate of the Liulin section determined by the magnetostratigraphy.

sp. existed in the Miocene, whereas the most ancient *Meriones* representatives lived during the Pleistocene and the origin of ancestral *Meriones* was set to the Pliocene (Chevret & Bobigny, 2005; Dianat et al., 2017; Wang et al., 2013). Therefore, the chronology presented in Anwar et al. (2015) and Zhang et al. (2018, 2022) is consistent with the Pliocene-Pleistocene age for the SL section. We note that the bottom of the SL red clay is not exposed in the outcrop and in the future it is possible to reach the late Miocene red clay layers using drilling. The LL section is older than the SL section considering the fossil evidence from both SL and LL that is supported by the magnetostratigraphy.

The LL section is located in a valley with a lower elevation compared to the SL section and has a ~400 m height difference with a 40 km horizontal separation of the sections (Figure 1b). Taking it into account we combined both records that have overlapped each other into a long magnetic susceptibility (LMS) record spanning from the Gauss chron to C3A chron (Figure 7). Both MS records were stacked together by averaging the values between two parts in the overlapping interval of 5.2–4 Ma. Figure 7 demonstrates similarities of the general long-term trends between LMS and the JC section MS record (Ding et al., 2001), while smaller-scale features differ in the terms of amplitudes.

## 4. Discussion

### 4.1. Discovery of the 1.2 Myr Cycle in the Asian Monsoon Record

The typical changes of MS records in the eolian sediments of CLP are well known for their close match with the global glacial-interglacial cycles depicted by the  $\delta^{18}\text{O}$  records in marine sediments and by the time-series of summer insolation at  $65^\circ\text{N}$  derived from orbital solutions (Laskar et al., 2004). We obtained independent climate records from terrestrial archives of CLP in order to reconstruct the atmospheric circulation in eastern Asia since the late Miocene. We compared our stacked LMS record from the eastern part of CLP with the inland JC red clay section (Figures 7a–7d; Ding et al., 2001).

The results of the wavelet analysis of the LMS record show a clear 405 Kyr eccentricity cycle between 7 and 2.5 Ma (Figure 7e) which is linked to the gravitational interaction of Jupiter and Venus ( $g_2$ – $g_5$ ), while the MS in the central CLP indicates an accentuation of the 405 Kyr band between 4 and 2.5 Ma (Figure 7f). Interestingly,

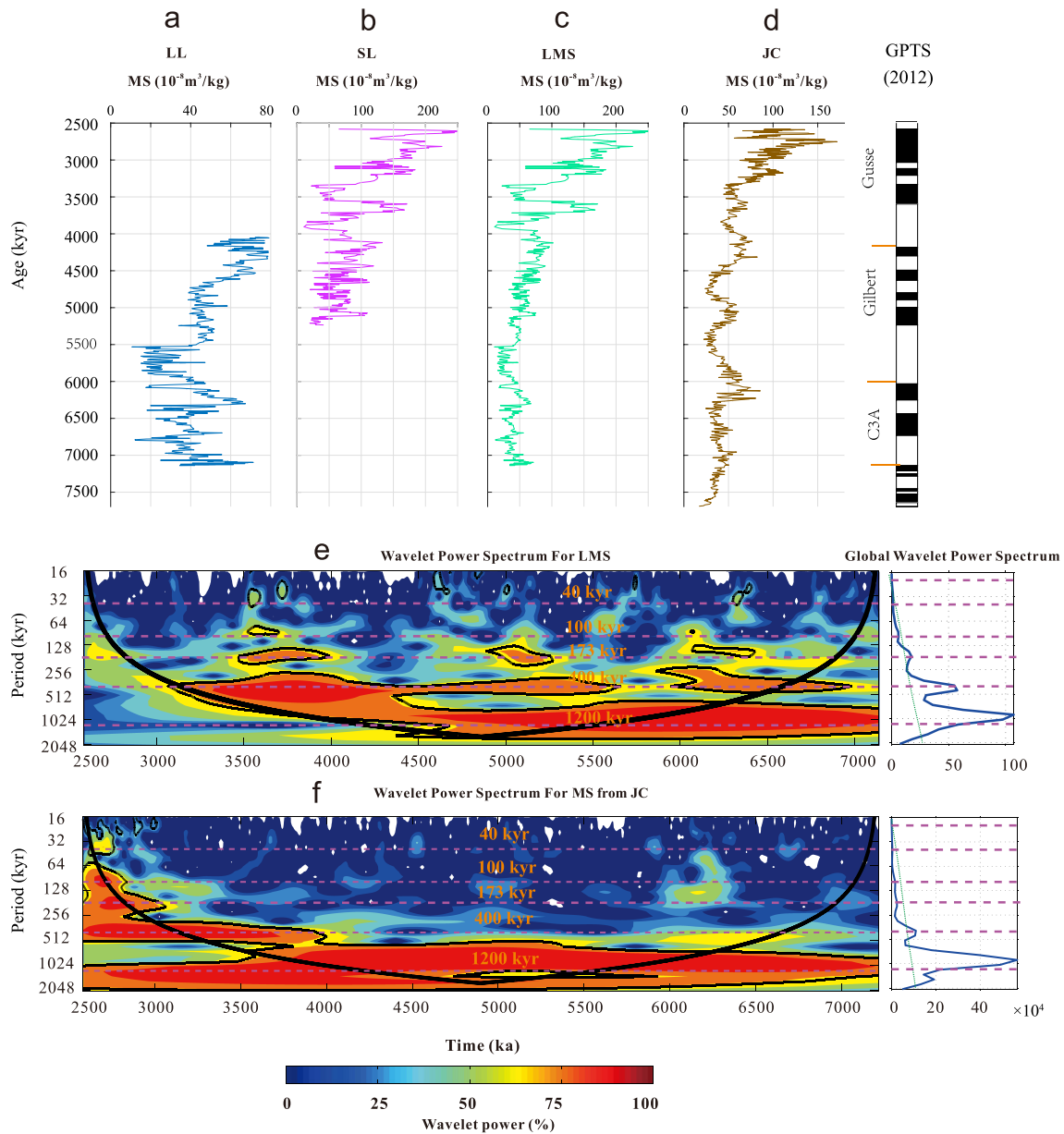


**Figure 7.** Comparison of magnetic susceptibility as a function of age from red clay sections in the Chinese Loess Plateau. Three stages of different climate conditions as shown by the magnetic susceptibility (MS). (a) MS of the Liulin (LL) red clay section. (b) MS of the Shilou (SL) red clay section (Anwar et al., 2015). (c) Long magnetic susceptibility (LMS) of the combined LL and SL red clay sections. (d) MS of the Jingchuan (JC) red clay section (Ding et al., 2001). (e) Wavelet analysis of magnetic susceptibility records from the LMS. (f) Wavelet spectrum of magnetic susceptibility from the JC section.

a  $\sim 1.2$  Myr grand cycle of  $s_4 - s_3$  obliquity modulation, linked to the orbital inclination rates of Mars and Earth, is superimposed with the 405 and 100 Kyr bands (Figures 7e and 7f) similarly to previous climatic records (van Dam et al., 2006) and is interpreted as beats between secular frequencies  $p + s_4$  and  $p + s_3$  (Laskar et al., 2004). The chaotic solar system has two major secular resonances. The first argument,  $\theta = (s_4 - s_3) - 2(s_4 - g_3)$  draws particular attention because the two longest orbital secular frequencies, obliquity and precession modulations, from  $s_4 - s_3$  to  $g_4 - g_3$  ( $\sim 2.4$  Myr) experienced intermittent chaotic transitions at  $\sim 2:1$  resonance states, when  $\sim 1.2$  Myr cycle dominates since 50 Ma (Crampton et al., 2018; Hinnov, 2000; Laskar et al., 2004; Palike et al., 2004).

To further highlight the expression of the 405 and 100 Kyr eccentricity bands within the LMS and JS records, we applied a two-channel band-pass filter with 350–500 and 80–125 Kyr bandwidths, respectively (red curves

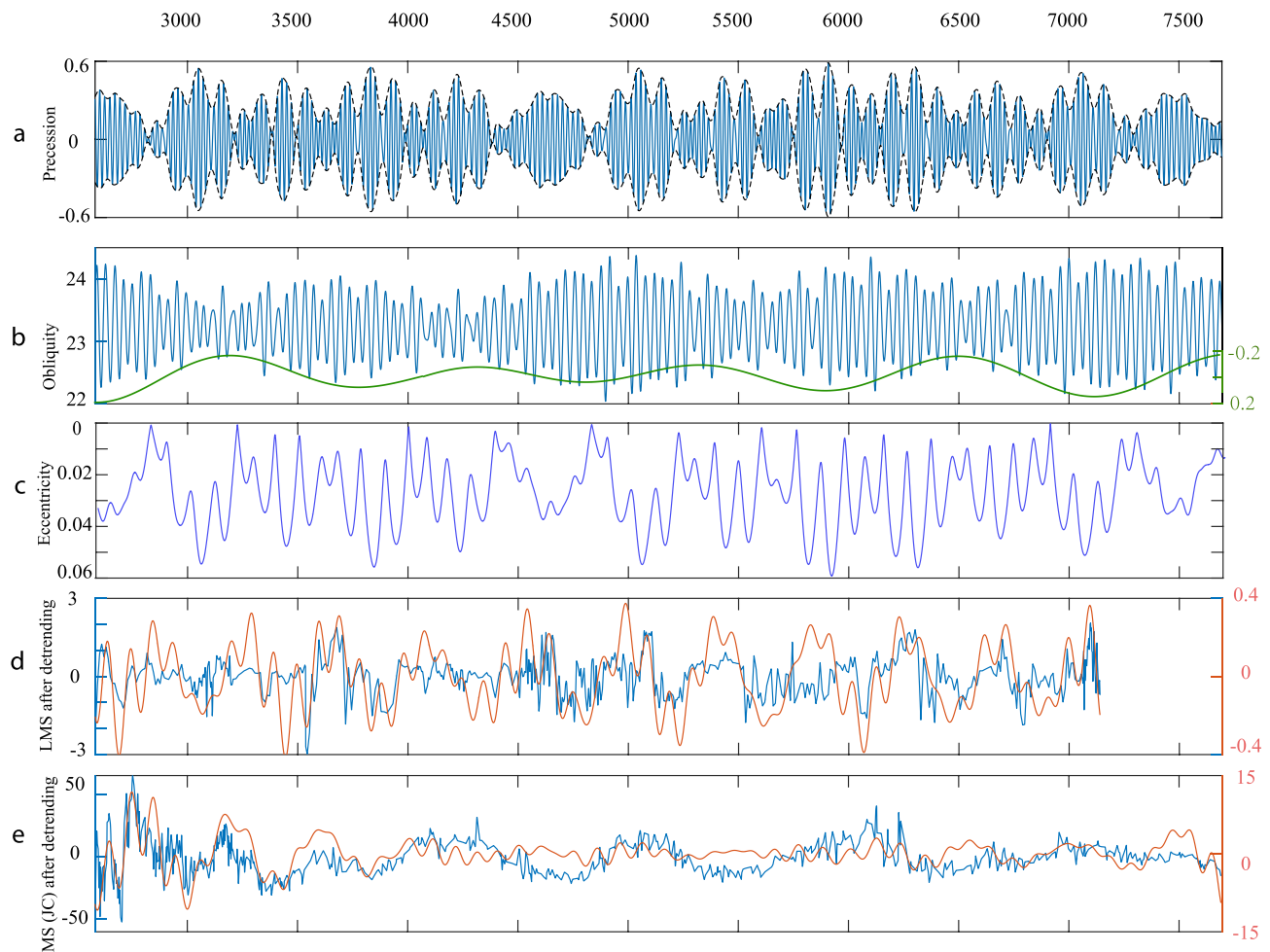


**Figure 8.** Milankovitch cycles between 7.8 and 2.5 Ma were derived from the astronomical solution (Laskar et al., 2004) and the Asian monsoon record. (a) Amplitude modulation of the precession solution (blue line) with its envelope curve (black dashed line) with the  $\sim 100,000$  and  $\sim 405,000$  cycles. (b) The  $\sim 1.2$  Myr amplitude modulation (green line) of the obliquity solution (Laskar et al., 2004; blue line). (c) Eccentricity solution (Laskar et al., 2004). (d) Long magnetic susceptibility (LMS) is detrended by the Lowess smoothing method (blue). (e) Magnetic susceptibility from Jingchuan (JC) section after detrending using the Lowess smoothing method (blue) (Ding et al., 2001). Red lines indicate the two-band filter with bandwidths of 350–500 and 80–125 Kyr in (d, e).

in Figure 8) after removing the long-term trend that could be related to tectonic processes in the region (Anwar et al., 2015; Zhang, Kravchinsky, et al., 2021; Zhang et al., 2022). The minima of each 405 Kyr cycle after the filter application between  $\sim 5.3$  and 2.5 Ma for both MS curves (Figures 8d and 8e) correlate with the eccentricity maxima (Figure 8c). However, prior to this period, the curves are out of phase suggesting that some other signal should have affected the climate variations during the late Miocene. In contrast to the filtered signals and astronomical cycles (red solid and green dashed lines), the unfiltered MS (Figures 8d and 8e) curves show less variability but the conspicuous grand cycle related to the 1.2 Myr obliquity modulation is evident between 7.1 and 4 Ma.

#### 4.2. Global Documentation of the 1.2 Myr Cycle That Drives the Miocene-Pliocene Climate Variations

Obliquity, precession and their modulations have been shown to be important driving forces of the global monsoon system which is sensitive to change in insolation, waxing and waning of ice sheets, and  $\text{CO}_2$  concentration (Anwar et al., 2015; Nie, 2018; Nie et al., 2008; Prell & Kutzbach, 1992; Zhang et al., 2022). Various time series, such as MS,  $\delta^{18}\text{O}$ , SST, and atmospheric  $\text{CO}_2$  levels, display a significant climatic transition at  $\sim 5.3$  Ma (Beerling & Royer, 2011; Herbert et al., 2016; Holbourn et al., 2018; Liu et al., 2019; Tian et al., 2008; Figure 9). The MS records show that the intensification of the Tibetan Plateau rise enhanced the 405 Kyr band by a strengthened

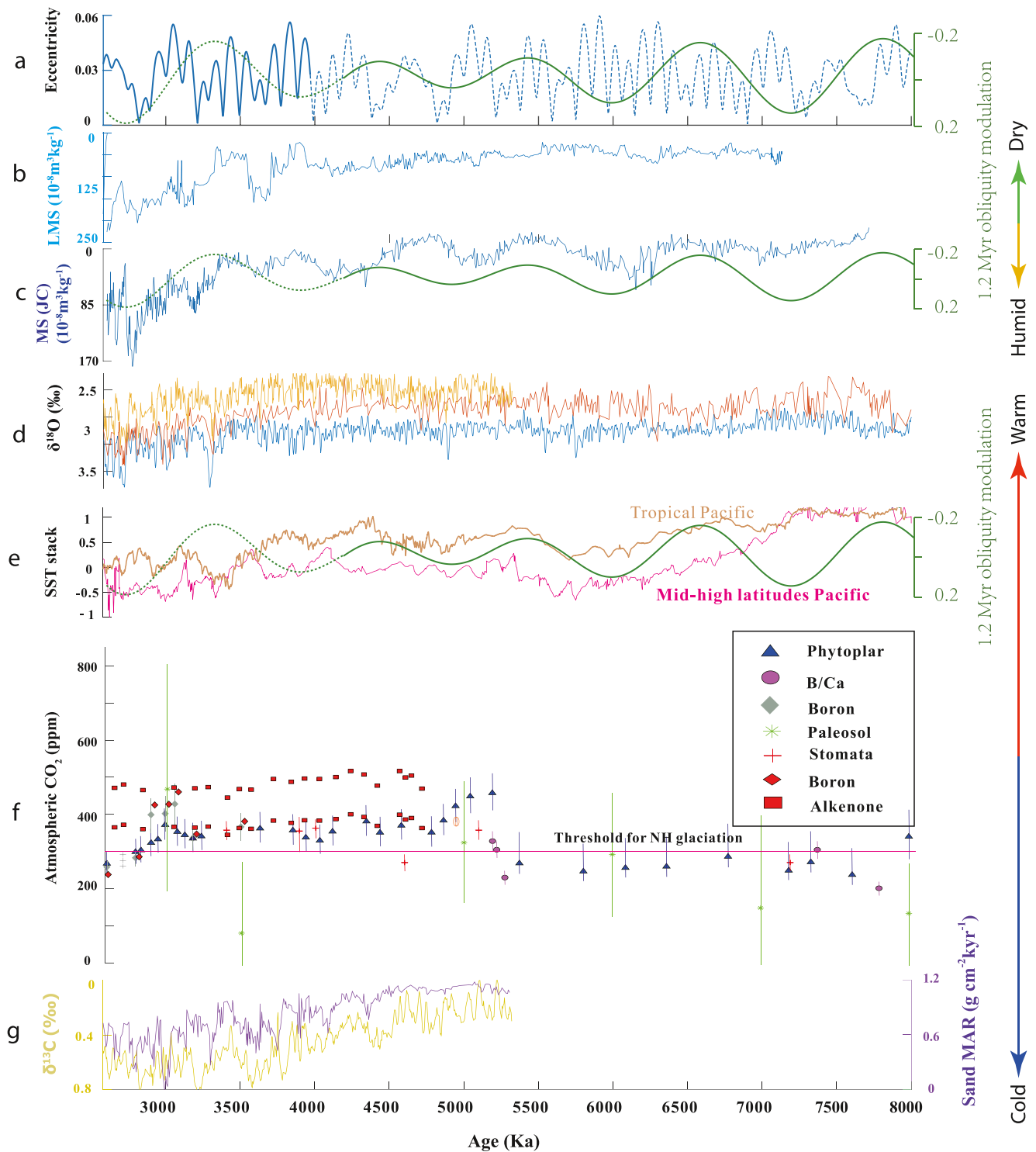
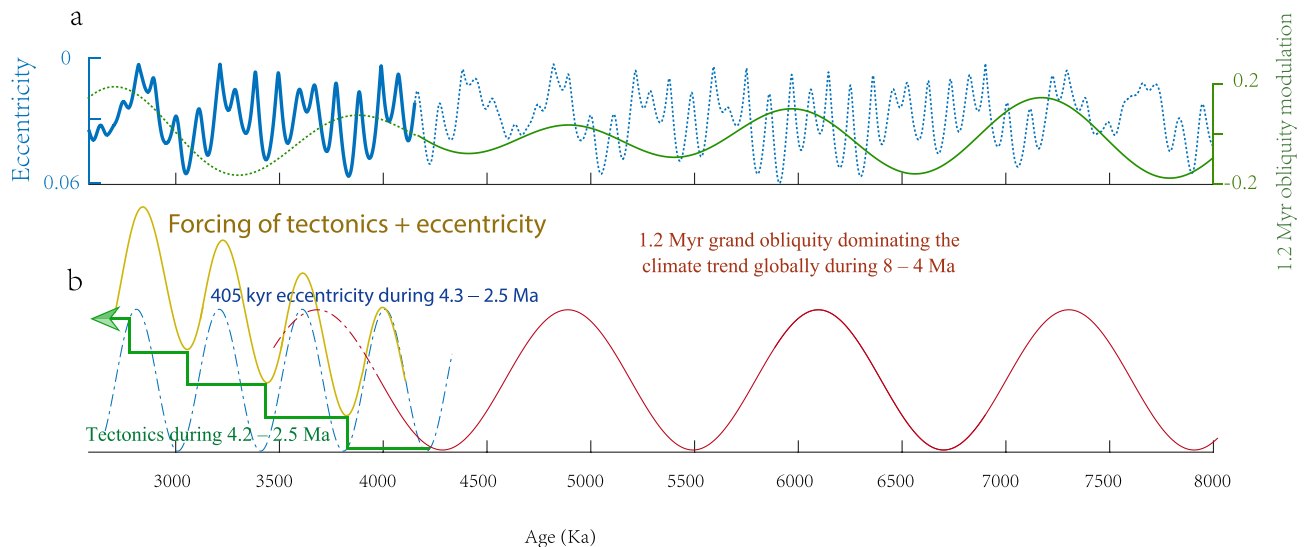


Figure 9.

summer monsoon since  $\sim 3.6$ – $4.2$  Ma (Figures 9b and 9c; Nie et al., 2008). Therefore, we argue that tectonic processes that impacted regional land-sea heat exchanges strongly influence the orbital-sensitive climate fluctuations, which, in turn, induced significant changes in the insolation-forced summer monsoon and led to introducing the tectonic related long-term trend toward two-three times higher values of MS in the interval between  $\sim 4.2$  and  $3.6$  Ma (Figures 9b and 9c). In the ocean, the negative shifts of benthic  $\delta^{18}\text{O}$  records (Figure 9d) correspond





**Figure 10.** The simplified climate model for Asian monsoon from late Miocene to Pliocene. (a) Eccentricity solution (Laskar et al., 2004) (blue solid and dashed lines), and the ~1.2 Myr obliquity modulation (green solid line from 8 to 4 Ma and green dashed line from 4 to 2.5 Ma). (b) Mathematical model showing the 1.2 Myr grand cycles (red) during the 8 to 4 Ma ( $Y1 = \cos(2 \times \pi \times (1/1,200) \times t)$ ); the 400 eccentricity cycles (blue) ( $Y2 = \sin(2 \times \pi \times (1/400) \times t)$ ) and the stepped tectonics (green arrow;  $Y3$ ) during the 4–2.5 Ma; compound of long eccentricity and stepped tectonics (yellow;  $Y4 = Y2 \times Y3$ ).

to the decrease of MS (Figures 9b and 9c). In contrast, the positive shifts of  $\delta^{18}\text{O}$  (Figure 9d) and the increase of MS (Figures 9b and 9c) and SST (Figure 9) correspond to a global cooling and inland aridification that led to the birth of the Sahara and Taklimakan deserts ~7 Ma (Schuster et al., 2006; J. Sun et al., 2009).

Previous studies have pointed out that a strengthened winter monsoon during the 7.1–5.5 Ma time interval was associated with an expansion of ice sheets in the Northern Hemisphere (Holbourn et al., 2018; Thiede et al., 1998; Wolf-Wellington et al., 1996) and indicated a global cooling during the Late Miocene (Zachos et al., 2001). The  $\delta^{18}\text{O}$  record of benthic foraminifera showed a clear decrease indicating a warming transition ~5.5–5.3 Ma (Holbourn et al., 2018; Westerhold et al., 2020). Such interpretation of both climatic variations at ~7 and 5.3 Ma is supported by the variability of the 1.2 Ma obliquity modulation (Figures 9a and 10) during the 7.6–3.6 Ma intervals. The grand obliquity curve is on the descent at 7 Ma and on the rise at 5.3 Ma. Several lines of evidence indicate that the closure of the Panama and Indonesia seaways may have also caused a significant reorganization of ocean circulation and increased the Gulf Stream yielding substantial transfer of warm and saline water masses to high northern latitudes during the Miocene-Pliocene between 6 and 2.7 Ma (Cane & Molnar, 2001; Haug et al., 2001). The warm conditions at high latitudes (Figure 9) may result from the massive input of warmer water. The planktonic foraminifera isotopic records from the Caribbean Sea indicate that salinity of the Caribbean surface waters already started to increase at the beginning of Pliocene, suggesting a weakened surface water circulation between the tropical Atlantic and Pacific Oceans as a result of the growth of the Central American isthmus of Panama (Haug & Tiedemann, 1998). It probably led to a climate pattern of a 405 Kyr cycle in the Western Hemisphere even earlier than the Asian Monsoon region (Figure 9g; Nie, 2018). However, there is still controversy, to determine when the seaway closed, if not possible, until the “Great American Exchange” of Vertebrates between North and South America that occurred ~2.7–2.6 Ma (Molnar, 2008). On the other hand, the thickening of the equatorial Western Pacific warm pool triggered by the closure of the Panama and Indonesian seaways may have expanded the exchanges of heat and moisture toward high latitudes. This process contributed to the warming

**Figure 9.** Compilation of Asian monsoon and global climatic proxies. (a) Illustration of the eccentricity solution (Laskar et al., 2004) (blue solid and dashed lines) and the ~1.2 Myr grand cycles/obliquity modulation (red solid and dashed line). (b) Combined long magnetic susceptibility (LMS) record of the Liulin (LL) and Shilou (SL) sections. (c) Magnetic susceptibility (MS) from Jingchuan (JC) section in the central Chinese Loess Plateau (CLP; Ding et al., 2001). (d) Benthic  $\delta^{18}\text{O}$  global record (Westerhold et al., 2020; blue) and benthic  $\delta^{18}\text{O}$  record from ODP Site 1148 (Tian et al., 2008) (red) and  $\delta^{18}\text{O}$  from ODP Site 999 (Haug & Tiedemann, 1998). (e) Stacked sea-surface temperature (SST) from mid-high (pink) and tropical (brown) latitudes. Pacific mid-high latitude records are integrated from DSDP Site 594, ODP Sites 883/884, 887, 1010, 1012, 1021, 1125, and 1208; Pacific tropical records are integrated from the IODP Sites U1337, U1338, ODP Sites 846, 847, 850 and 1241 (Liu et al., 2019). (f) Atmospheric  $\text{CO}_2$  history during the past 8 Myr from different proxies (Beerling & Royer, 2011; Herbert et al., 2016). The horizontal red line indicates the Northern Hemisphere glaciation threshold (approx. 280 ppm). (g)  $\delta^{13}\text{C}$  record (yellow) and carbonate sand-fraction mass accumulation rates (purple) from ODP site 999 (Haug & Tiedemann, 1998).

up of the South China Sea water and to increase the precipitation on the Asian continent (Li et al., 2008; Yan et al., 1992). The gradual growth of the Tibetan Plateau ~4.2 Ma may have also increased the air pressure gradient between land and sea, resulting in greater seasonal precipitation within the monsoon influence region. The 1.2 and 0.405 Myr long amplitude modulations of the obliquity and precession cycles are prominent features of the climate pattern between the late Miocene and Pliocene, especially for the Asian monsoon.

## 5. Conclusions

Our interpretation of the LMS record shows that the Asian summer monsoon appears to be orbitally controlled by the 1.2 Myr grand obliquity cycle band between 7.7 and 4 Ma and by the 0.405 Myr long eccentricity band between 4 and 2.5 Ma. We conclude that global cooling and warming that occurred 7 and 5.3 Ma respectively, as well as the Antarctic ice volume, carbon cycle dynamics, and the monsoon forcing of the upper-ocean circulation were all triggered by the grand obliquity variations before the middle Pliocene. Since then, a series of major tectonic events such as the closure of the Panama and Indonesian seaways and the uplift of the Tibetan Plateau, accelerated the transition from a 1.2 Myr obliquity-dominated to a 0.405 Myr eccentricity-dominated climate variability for the Asian monsoon.

## Conflict of Interest

The authors declare no conflicts of interest relevant to this study.

## Data Availability Statement

The data are available at <https://doi.org/10.5281/zenodo.6391476>.

## Acknowledgments

This study was funded by the National Natural Science Foundation of China (41772027, 41972035, and 41950410574) for R.Z., J.Q. and J.L., the China Scholarship Council for J.Q. (202006970027), and the Natural Sciences and Engineering Research Council of Canada (NSERC grant RGPIN-2019-04780) for V.A.K. The authors thank two anonymous reviewers and an associate editor for their valuable comments that helped to substantially improve the manuscript. Rui Zhang and Vadim A. Kravchinsky prepared the manuscript with intellectual contributions from all authors.

## References

- An, Z., Kutzbach, J. E., Prell, W. L., & Porter, S. C. (2001). Evolution of Asian monsoons and phased uplift of the Himalaya-Tibetan plateau since late Miocene times. *Nature*, 411, 62–66. <https://doi.org/10.1038/35075035>
- Anwar, T., Kravchinsky, V. A., & Zhang, R. (2015). Magneto- and cyclostratigraphy in the red clay sequence: New age model and paleoclimatic implication for the eastern Chinese Loess Plateau. *Journal of Geophysical Research: Solid Earth*, 120, 6758–6770. <https://doi.org/10.1002/2015JB012132>
- Ao, H., Roberts, A. P., Dekkers, M. J., Liu, X., Rohling, E. J., Shi, Z., et al. (2016). Late Miocene-Pliocene Asian monsoon intensification linked to Antarctic ice-sheet growth. *Earth and Planetary Science Letters*, 444, 75–87. <https://doi.org/10.1016/j.epsl.2016.03.028>
- Badgley, C., Barry, J. C., Morgan, M. E., Nelson, S. V., Behrensmeyer, A. K., Cerling, T. E., & Pilbeam, D. (2008). Ecological changes in Miocene mammalian record show impact of prolonged climatic forcing. *Proceedings of the National Academy of Sciences*, 105, 12145–12149. <https://doi.org/10.1073/pnas.0805592105>
- Beerling, D. J., & Royer, D. L. (2011). Convergent Cenozoic CO<sub>2</sub> history. *Nature Geoscience*, 4, 418–420. <https://doi.org/10.1038/ngeo1186>
- Bolton, C. T., & Stoll, H. M. (2013). Late Miocene threshold response of marine algae to carbon dioxide limitation. *Nature*, 500, 558–562. <https://doi.org/10.1038/nature12448>
- Boos, W. R., & Kuang, Z. (2010). Dominant control of the South Asian monsoon by orographic insulation vs. plateau heating. *Nature*, 463, 218–222. <https://doi.org/10.1038/nature08707>
- Burke, K. D., Williams, J. W., Chandler, M. A., Haywood, A. M., Lunt, D. J., & Otto-Bliesner, B. L. (2018). Pliocene and Eocene provide best analogs for near-future climates. *Proceedings of the National Academy of Sciences*, 115, 13288–13293. <https://doi.org/10.1073/pnas.1809600115>
- Cane, M. A., & Molnar, P. (2001). Closing of the Indonesian seaway as a precursor to east African aridification around 3–4 Myr ago. *Nature*, 411, 157–162. <https://doi.org/10.1038/35075500>
- Cerling, T. E., Harris, J. M., MacFadden, B. J., Leakey, M. G., Quade, J., Eisenmann, V., & Ehleringer, J. R. (1997). Global vegetation change through the Miocene/Pliocene boundary. *Nature*, 389, 153–158. <https://doi.org/10.1038/38229>
- Chevret, P., & Bobigny, G. (2005). Systematics and evolution of the subfamily Gerbillinae (Mammalia, Rodentia, Muridae). *Molecular Phylogenetics and Evolution*, 35, 674–688. <https://doi.org/10.1016/j.ympev.2005.01.001>
- Crampton, J. S., Meyers, S. R., Cooper, R. A., Sadler, P. M., Foote, M., & Harte, D. (2018). Pacing of Paleozoic macroevolutionary rates by Milankovitch grand cycles. *Proceedings of the National Academy of Sciences*, 115, 5686–5691. <https://doi.org/10.1073/pnas.1714342115>
- Dianat, M., Darvish, J., Cornette, R., Aliabadian, M., & Niolas, V. (2017). Evolutionary history of the Persian Jird, *Meriones persicus*, based on genetics, species distribution modeling, and morphometric data. *Journal of Zoological Systematics and Evolutionary Research*, 55, 29–45. <https://doi.org/10.1111/jzs.12145>
- Ding, Z., Yang, S., Hou, S., Wang, X., Chen, Z., & Liu, T. (2001). Magnetostratigraphy and sedimentology of the Jingchuan red clay section and correlation of the Tertiary eolian red clay sediments of the Chinese Loess Plateau. *Journal of Geophysical Research: Solid Earth*, 106, 6399–6407. <https://doi.org/10.1029/2000JB900445>
- Dowsett, H. J., Chandler, M. A., Cronin, T. M., & Dwyer, G. S. (2005). Middle Pliocene sea surface temperature variability. *Paleoceanography*, 20, PA2014. <https://doi.org/10.1029/2005PA001133>
- Fedorov, A. V., Dekens, P. S., McCarthy, M., Ravelo, A. C., deMenocal, P. B., Barreiro, M., et al. (2006). The Pliocene paradox (mechanisms for a permanent El Niño). *Science*, 312, 1485–1489. <https://doi.org/10.1126/science.1122666>

- Hao, Q., Wang, L., Oldfield, F., Peng, S., Qin, L., Song, Y., et al. (2012). Delayed build-up of Arctic ice sheets during 400,000 yr minima in insolation variability. *Nature*, 490, 393–396. <https://doi.org/10.1038/nature11493>
- Haug, G. H., & Tiedemann, R. (1998). Effect of the formation of the isthmus of Panama on Atlantic Ocean thermohaline circulation. *Nature*, 393, 673–676. <https://doi.org/10.1038/31447>
- Haug, G. H., Tiedemann, R., Zahn, R., & Ravelo, A. C. (2001). Role of Panama uplift on oceanic freshwater balance. *Geology*, 29, 207–210. [https://doi.org/10.1130/0091-7613\(2001\)029<0207:ROPUOO>2.0.CO;2](https://doi.org/10.1130/0091-7613(2001)029<0207:ROPUOO>2.0.CO;2)
- Herbert, T. D., Lawrence, K. T., Tzanova, A., Peterson, L. C., Caballero-Gill, R., & Kelly, C. S. (2016). Late Miocene global cooling and the rise of modern ecosystems. *Nature Geoscience*, 9, 843–847. <https://doi.org/10.1038/ngeo2813>
- Hinnov, L. A. (2000). New perspectives on orbitally forced stratigraphy. *Annual Review of Earth and Planetary Sciences*, 28, 419–475. <https://doi.org/10.1146/annurev.earth.28.1.419>
- Holbourn, A. E., Kuhnt, W., Clemens, S. C., Kochhann, K. G., Jöhnck, J., Lübbers, J., & Andersen, N. (2018). Late Miocene climate cooling and intensification of southeast Asian winter monsoon. *Nature Communications*, 9, 1584. <https://doi.org/10.1038/s41467-018-03950-1>
- Huang, Y., Clemens, S. C., Liu, W., Wang, Y., & Prell, W. L. (2007). Large-scale hydrological change drove the late Miocene C4 plant expansion in the Himalayan foreland and Arabian Peninsula. *Geology*, 35, 531–534. <https://doi.org/10.1130/G23666A.1>
- Krischvink, J. L. (1980). The least squares line and plane and the analysis of paleomagnetic data. *Geophysical Journal International*, 62, 699–718. <https://doi.org/10.1111/j.1365-246X.1980.tb02601.x>
- LaRiviere, J. P., Ravelo, A. C., Crimmins, A., Dekens, P. S., Ford, H. L., Lyle, M., & Wara, M. W. (2012). Late Miocene decoupling of oceanic warmth and atmospheric carbon dioxide forcing. *Nature*, 486, 97–100. <https://doi.org/10.1038/Nature11200>
- Laskar, J. (2020). Astrochronology. In F. M. Gradstein, J. G. Ogg, M. D. Schmitz, & G. M. Ogg (Eds.), *The geologic time scale 2020* (pp. 139–158). Elsevier.
- Laskar, J., Correia, A. C. M., Gastineau, M., Joutel, F., Levrard, B., & Robutel, P. (2004). Long term evolution and chaotic diffusion of the insolation quantities of Mars. *Icarus*, 170, 343–364. <https://doi.org/10.1016/j.icarus.2004.04.005>
- Lawrence, K. T., Liu, Z., & Herbert, T. D. (2006). Evolution of the eastern tropical Pacific through Plio-Pleistocene glaciation. *Science*, 312, 79–83. <https://doi.org/10.1126/science.1120395>
- Lewis, A. R., Marchant, D. R., Ashworth, A. C., Hedenäs, L., Hemming, S. R., Johnson, J. V., et al. (2008). Mid-Miocene cooling and the extinction of tundra in continental Antarctica. *Proceedings of the National Academy of Sciences*, 105, 10676–10680. <https://doi.org/10.1073/pnas.0802501105>
- Li, F., Rousseau, D. D., Wu, N., Hao, Q., & Pei, Y. (2008). Late Neogene evolution of the East Asian monsoon revealed by terrestrial mollusk record in Western Chinese Loess Plateau: From winter to summer dominated sub-regime. *Earth and Planetary Science Letters*, 274, 439–447. <https://doi.org/10.1016/j.epsl.2008.07.038>
- Liu, J., Tian, J., Liu, Z., Herbert, T. D., Fedorov, A. V., & Lyle, M. (2019). Eastern equatorial Pacific cold tongue evolution since the late Miocene linked to extratropical climate. *Science Advances*, 5, eaau6060. <https://doi.org/10.1126/sciadv.aau6060>
- Molnar, P. (2008). Closing of the Central American seaway and the ice age: A critical review. *Paleoceanography and Paleoclimatology*, 23. <https://doi.org/10.1029/2007PA001574>
- Naish, T., Powell, R., Levy, R., Wilson, G., Scherer, R., Talarico, F., et al. (2009). Obliquity-paced Pliocene West Antarctic ice sheet oscillations. *Nature*, 458, 322–329. <https://doi.org/10.1038/nature07867>
- Nie, J. (2018). The Plio-Pleistocene 405 Kyr climate cycles. *Paleogeography, Paleoclimatology, Paleocology*, 510, 26–30. <https://doi.org/10.1016/j.palaeo.2017.07.022>
- Nie, J., King, J. W., & Fang, X. (2008). Tibetan uplift intensified the 400 Kyr signal in paleoclimate records at 4 Ma. *Geological Society of America Bulletin*, 120, 1338–1344. <https://doi.org/10.1130/B26349.1>
- Ogg, J. G. (2012). Geomagnetic polarity time scale. In F. M. Gradstein, J. G. Ogg, M. D. Schmitz, & G. M. Ogg (Eds.), *The geologic time scale 2012* (pp. 85–113). Elsevier.
- Palike, H., Laskar, J., & Shackleton, N. J. (2004). Geologic constraints on the chaotic diffusion of the solar system. *Geology*, 32, 929–932. <https://doi.org/10.1130/G20750.1>
- Prell, W. L., & Kutzbach, J. E. (1992). Sensitivity of the Indian monsoon to forcing parameters and implications for its evolution. *Nature*, 360, 647–652. <https://doi.org/10.1038/360647a0>
- Ravelo, A. C., Andreasen, D. H., Lyle, M., Lyle, A. O., & Wara, M. W. (2004). Regional climate shifts caused by gradual global cooling in the Pliocene epoch. *Nature*, 429, 263–267. <https://doi.org/10.1038/nature02567>
- Schuster, M., Düringer, P., Ghienne, J. F., Vignaud, P., Mackaye, H. T., Likies, A., & Brunet, M. (2006). The age of the Sahara Desert. *Science*, 311, 821. <https://doi.org/10.1126/science.1120161>
- Sun, J., Zhang, Z., & Zhang, L. (2009). New evidence on the age of the Taklimakan Desert. *Geology*, 37, 159–162. <https://doi.org/10.1130/G25338A.1>
- Sun, Y., Yin, Q., Crucifix, M., Clemens, S. C., Araya-Melo, P., Liu, W., et al. (2019). Diverse manifestations of the mid-Pleistocene climate transition. *Nature Communications*, 10, 352. <https://doi.org/10.1038/s41467-018-08257-9>
- Thiede, J., Winkler, A., Wolf-Welling, T., Eldholm, O., Myhre, A. M., Baumann, K. H., et al. (1998). Late Cenozoic history of the polar North Atlantic: Results from ocean drilling. *Quaternary Science Reviews*, 17, 185–208. [https://doi.org/10.1016/S0277-3791\(97\)00076-0](https://doi.org/10.1016/S0277-3791(97)00076-0)
- Tian, J., Zhao, Q., Wang, P., Li, Q., & Cheng, X. (2008). Astronomically modulated Neogene sediment records from the South China Sea. *Paleoceanography*, 26, PA3210. <https://doi.org/10.1029/2007pa001552>
- van Dam, J., Abdul Aziz, H., Alvarez Sierra, M. A., Hilgen, F. J., van den Hoek Ostende, L. W., Lourens, L. J., et al. (2006). Long-period astronomical forcing of mammal turnover. *Nature*, 443, 687–691. <https://doi.org/10.1038/nature05163>
- Wang, Y., Zhao, L., Fang, F., Liao, J., & Liu, N. (2013). Intraspecific molecular phylogeny and phylogeography of the Meriones meridianus (Rodentia: Cricetidae) complex in northern China reflect the processes of desertification and the Tianshan Mountains uplift. *Biological Journal of the Linnean Society*, 110, 362–383. <https://doi.org/10.1111/bj.12123>
- Westerhold, T., Marwan, N., Drury, A. J., Liebrand, D., Agnini, C., Anagnostou, E., et al. (2020). An astronomically dated record of Earth's climate and its predictability over the last 66 Myr. *Science*, 369, 1383–1387. <https://doi.org/10.1126/science.aba6853>
- Wolf-Welling, T. C., Cremer, M., O'Connell, S., Winkler, A., & Thiede, J. (1996). Cenozoic Arctic gateway paleoclimate variability: Indications from changes in coarse-fraction composition. *Proceedings of the Ocean Drilling Program, Scientific Results*, 151, 515–568. <https://doi.org/10.2973/odp.proc.sr.151.139.1996>
- Xu, Y., Yue, L., Li, J., Sun, L., Sun, B., Zhang, J., et al. (2009). An 11-Ma-old red clay sequence on the Eastern Chinese Loess Plateau. *Paleogeography, Paleoclimatology, Paleocology*, 284, 383–391. <https://doi.org/10.1016/j.palaeo.2009.10.023>
- Xu, Y., Yue, L., Li, J., Wang, J., Sun, B., Sun, L., et al. (2013). Late Neogene red clay in the Fuxing area of western foothills of the Lüliang Mountain. *Journal of Stratigraphy*, 37, 33–40. (in Chinese).

- Xu, Y., Yue, L. P., Li, J. X., Sun, L., Sun, B., Zhang, J. Y., et al. (2012). Red clay deposits on the Chinese Loess Plateau during 11.0–2.6 Ma and its implications for long-term evolution of East Asian monsoon. *Environmental Earth Sciences*, 66, 2021–2030.
- Yan, X., Ho, C., Zheng, Q., & Klemas, V. (1992). Temperature and size variabilities of the west Pacific warm pool. *Science*, 258, 1643–1645. <https://doi.org/10.1126/science.258.5088.1643>
- Zachos, J., Pagani, M., Sloan, L., Thomas, E., & Billups, K. (2001). Trends, rhythms, and aberrations in global climate 65 Ma to present. *Science*, 292, 686–693. <https://doi.org/10.1126/science.1059412>
- Zhang, R., Kravchinsky, V. A., Anwar, T., Yue, L., Li, J., & Jiao, J. (2018). Comment on “late Miocene-Pliocene Asian monsoon intensification linked to Antarctic ice-sheet growth” [Earth Planet. Sci. Lett. 444 (2016) 75–87]. *Earth and Planetary Science Letters*, 503, 75248–87251. <https://doi.org/10.1016/j.epsl.2018.08.033>
- Zhang, R., Kravchinsky, V. A., Qin, J., Goguitchaichvili, A., & Li, J. (2021). One and a half million year long aridity during the middle Eocene in North-West China linked to a global cooling episode. *Journal of Geophysical Research: Solid Earth*, 126, e2020JB021037. <https://doi.org/10.1029/2020JB021037>
- Zhang, R., Li, X., Xu, Y., Li, J., Sun, L., Yue, L., et al. (2022). The 173 Kyr obliquity cycle pacing the Asian monsoon in the eastern Chinese Loess Plateau from late Miocene to Pliocene. *Geophysical Research Letters*, 49, e2021GL097008. <https://doi.org/10.1029/2021GL097008>
- Zhang, R., Wei, X., Kravchinsky, V. A., Yue, L., Zheng, Y., Qin, J., et al. (2021). “Tiny wiggles” in the late Miocene red clay deposits in the north-east of the Tibetan Plateau. *Geophysical Research Letters*, 48, e2021GL093962. <https://doi.org/10.1029/2021GL093962>
- Zheng, S., & Zhang, Z. (2000). Late Miocene-early Pleistocene micromammals from Wenwangou of Lingtai, Gansu, China. *Vertebrata Palasiatica*, 38, 58–71. (in Chinese). <http://119.78.100.205/handle/311034/898>
- Zheng, S., & Zhang, Z. (2001). Late Miocene-early Pleistocene biogeography of the Leijiahe area, Lingtai, Gansu. *Vertebrata Palasiatica*, 39, 215–228. (in Chinese). <http://119.78.100.205/handle/311034/883>
- Zhu, Y., Zhou, L., Mo, D., Kaakinen, A., Zhang, Z., & Fortelius, M. (2008). A new magnetostratigraphic framework for late Neogene Hipparion red clay in the eastern Loess Plateau of China. *Paleogeography, Paleoclimatology, Paleoecology*, 268, 47–57. <https://doi.org/10.1016/j.palaeo.2008.08.001>

## References From the Supporting Information

- An, Z. (2000). The history and variability of the East Asian paleomonsoon climate. *Quaternary Science Reviews*, 19, 171–187. [https://doi.org/10.1016/S0277-3791\(99\)00060-8](https://doi.org/10.1016/S0277-3791(99)00060-8)
- An, Z., Kukla, G., Porter, S. C., & Xiao, J. (1991a). Late Quaternary dust flow on the Chinese Loess Plateau. *Catena*, 18, 125–132. [https://doi.org/10.1016/0341-8162\(91\)90012-M](https://doi.org/10.1016/0341-8162(91)90012-M)
- An, Z., Kukla, G., Porter, S. C., & Xiao, J. (1991b). Magnetic susceptibility evidence of monsoon variation on the Loess Plateau of central China during the last 130,000 yr. *Quaternary Research*, 36, 29–36. [https://doi.org/10.1016/0033-5894\(91\)90015-W](https://doi.org/10.1016/0033-5894(91)90015-W)
- Ao, H., Roberts, A. P., Dekkers, M. J., Liu, X., Rohling, E. J., Shi, Z., et al. (2018). Reply to Zhang et al Late Miocene-Pliocene magnetostratigraphy of the Shilou red clay on the eastern Chinese Loess Plateau. *Earth and Planetary Science Letters*, 503, 252–255. <https://doi.org/10.1016/j.epsl.2018.08.045>
- Ding, Z., Rutter, N., Han, J., & Liu, T. (1992). A coupled environmental system formed at about 2.5 Ma in East-Asia. *Paleogeography, Paleoclimatology, Paleoecology*, 94, 223–242. [https://doi.org/10.1016/0031-0182\(92\)90120-T](https://doi.org/10.1016/0031-0182(92)90120-T)
- Ding, Z., Sun, J., Liu, T., Zhu, R., Yang, S., & Guo, B. (1998). Wind-blown origin of the Pliocene red clay formation in the central Loess Plateau, China. *Earth and Planetary Science Letters*, 161, 135–143. [https://doi.org/10.1016/S0012-821X\(98\)00145-9](https://doi.org/10.1016/S0012-821X(98)00145-9)
- Ding, Z., Sun, J., Yang, S., & Liu, T. (1998). Preliminary magnetostratigraphy of a thick eolian red clay-loess sequence at Lingtai, the Chinese Loess Plateau. *Geophysical Research Letters*, 25, 1225–1228. <https://doi.org/10.1029/98GL00836>
- Ding, Z., Xiong, S., Sun, J., Yang, S., Gu, Z., & Liu, T. (1999). Pedostratigraphy and paleomagnetism of a ~7.0 Ma eolian loess-red clay sequence at Lingtai, Loess Plateau, north-central China and the implications for paleomonsoon evolution. *Paleogeography, Paleoclimatology, Paleoecology*, 152, 49–66. [https://doi.org/10.1016/S0031-0182\(99\)00034-6](https://doi.org/10.1016/S0031-0182(99)00034-6)
- Evans, M. E., Wang, Y., Rutter, N., & Ding, Z. (1991). Preliminary magnetostratigraphy of the red clay underlying the loess sequence at Baoji, China. *Geophysical Research Letters*, 18, 1409–1412. <https://doi.org/10.1029/91GL01800>
- Guo, Z., Ruddiman, W. F., Hao, Q., Wu, H., Qiao, Y., Zhu, R., et al. (2002). Onset of Asian desertification by 22 Myr ago inferred from loess deposits in China. *Nature*, 416, 159–163. <https://doi.org/10.1038/416159a>
- Hao, Q., & Guo, Z. (2004). Magnetostratigraphy of a late Miocene-Pliocene loess-soil sequence in the Western Loess Plateau in China. *Geophysical Research Letters*, 31. <https://doi.org/10.1029/2003GL019392>
- Heller, F., & Liu, T. (1982). Magnetostratigraphical dating of loess deposits in China. *Nature*, 300, 431–433. <https://doi.org/10.1038/300431a0>
- Kukla, G., & An, Z. (1989). Loess stratigraphy in central China. *Paleogeography, Paleoclimatology, Paleoecology*, 72, 203–225. [https://doi.org/10.1016/0031-0182\(89\)90143-0](https://doi.org/10.1016/0031-0182(89)90143-0)
- Lisiecki, L. E., & Lisiecki, P. A. (2002). Application of dynamic programming to the correlation of paleoclimate records. *Paleoceanography*, 17, 1–11. <https://doi.org/10.1029/2001PA000733>
- Lisiecki, L. E., & Raymo, M. E. (2005). A Pliocene-Pleistocene stack of 57 globally distributed benthic  $\delta^{18}\text{O}$  records. *Paleoceanography and Paleoclimatology*, 20. <https://doi.org/10.1029/2004PA001071>
- Liu, T. (1985). *Loess and environment* (pp. 31–67). China Ocean Press.
- Qiang, X., An, Z., Song, Y., Chang, H., Sun, Y., Liu, W., et al. (2011). New eolian red clay sequence on the western Chinese Loess Plateau linked to onset of Asian desertification about 25 Ma ago. *Science China Earth Sciences*, 54, 136–144. <https://doi.org/10.1007/s11430-010-4126-5>
- Qiang, X., Li, Z., Powell, C. M., & Zheng, H. (2001). Magnetostratigraphic record of the late Miocene onset of the East Asian monsoon, and Pliocene uplift of northern Tibet. *Earth and Planetary Science Letters*, 187, 83–93. [https://doi.org/10.1016/S0012-821X\(01\)00281-3](https://doi.org/10.1016/S0012-821X(01)00281-3)
- Rutter, N., Ding, Z., Evans, M. E., & Liu, T. (1991). Baoji-type pedostratigraphic section, Loess Plateau, north-central China. *Quaternary Science Reviews*, 10, 1–22. [https://doi.org/10.1016/0277-3791\(91\)90028-S](https://doi.org/10.1016/0277-3791(91)90028-S)
- Song, Y., Fang, X., Chen, X., Torii, M., Ishikawa, N., Zhang, M., et al. (2018). Rock magnetic record of late Neogene red clay sediments from the Chinese Loess Plateau and its implications for East Asian monsoon evolution. *Paleogeography, Paleoclimatology, Paleoecology*, 510, 109–123. <https://doi.org/10.1016/j.palaeo.2017.09.025>
- Song, Y., Fang, X., Torii, M., Ishikawa, N., Li, J., & An, Z. (2007). Late Neogene rock magnetic record of climatic variation from Chinese eolian sediments related to uplift of the Tibetan Plateau. *Journal of Asian Earth Sciences*, 30, 324–332. <https://doi.org/10.1016/j.jseas.2006.10.004>
- Sun, D., An, Z., Shaw, J., Bloemendal, J., & Sun, Y. (1998). Magnetostratigraphy and paleoclimatic significance of late Tertiary aeolian sequences in the Chinese Loess Plateau. *Geophysical Journal International*, 134, 207–212. <https://doi.org/10.1046/j.1365-246X.1998.00553.x>



- Sun, D., John, S., An, Z., Cheng, M., & Yue, L. (1998). Magnetostratigraphy and paleoclimatic interpretation of a continuous 7.2 Ma late Cenozoic eolian sediments from the Chinese Loess Plateau. *Geophysical Research Letters*, 25, 85–88. <https://doi.org/10.1029/97GL03353>
- Sun, Y., An, Z., Clemens, S. C., Bloemendal, J., & Vandenberghe, J. (2010). Seven million years of wind and precipitation variability on the Chinese Loess Plateau. *Earth and Planetary Science Letters*, 297, 525–535. <https://doi.org/10.1016/j.epsl.2010.07.004>
- Torrence, C., & Compo, G. P. (1998). A practical guide to wavelet analysis. *Bulletin of the American Meteorological Society*, 79, 61–78. [https://doi.org/10.1175/1520-0477\(1998\)079<0061:APGTWA>2.0.CO;2](https://doi.org/10.1175/1520-0477(1998)079<0061:APGTWA>2.0.CO;2)
- Zheng, H., An, Z., & Shaw, J. (1992). New contributions to Chinese Plio-Pleistocene magnetostratigraphy. *Physics of the Earth and Planetary Interiors*, 70, 146–153. [https://doi.org/10.1016/0031-9201\(92\)90177-W](https://doi.org/10.1016/0031-9201(92)90177-W)

## Supplementary Material

for the manuscript

### **1.2-million-year band of Earth–Mars obliquity modulation on the evolution of cold late Miocene to warm early Pliocene climate**

Jie Qin<sup>1,2</sup>, Rui Zhang<sup>1,2,\*</sup>, Vadim A. Kravchinsky<sup>1,2,\*</sup>, Jean-Pierre Valet<sup>1,3</sup>, Leonardo Sagnotti<sup>4</sup>,  
Jianxing Li<sup>5</sup>, Yong Xu<sup>6</sup>, Taslima Anwar<sup>1,2</sup>, Leping Yue<sup>1</sup>

<sup>1</sup>Institute of Cenozoic Geology and Environment, State Key Laboratory of Continental Dynamics, Department of Geology, Northwest University, 710069 Xi'an, China

<sup>2</sup>Geophysics, Department of Physics, University of Alberta, T6G2E1 Edmonton, Canada

<sup>3</sup>Institut de Physique du Globe de Paris, 75238 Paris cedex 05, France

<sup>4</sup>Istituto Nazionale di Geofisica e Vulcanologia, 00143 Roma, Italy

<sup>5</sup>Chengdu Center of Geological Survey, Geological Survey of China, 610081 Chengdu, China

<sup>6</sup>Xi'an Center of Geological Survey, China Geological Survey, 710054 Xi'an, China

---

\* Correspondence to: R. Zhang and V.A. Kravchinsky,  
[ruizhang@nwu.edu.cn](mailto:ruizhang@nwu.edu.cn); [vadim@ualberta.ca](mailto:vadim@ualberta.ca)

This PDF file includes:

Supplementary Material Text S1– S3

Supplementary Material Figs. 1–4

References

## **S1 Introduction**

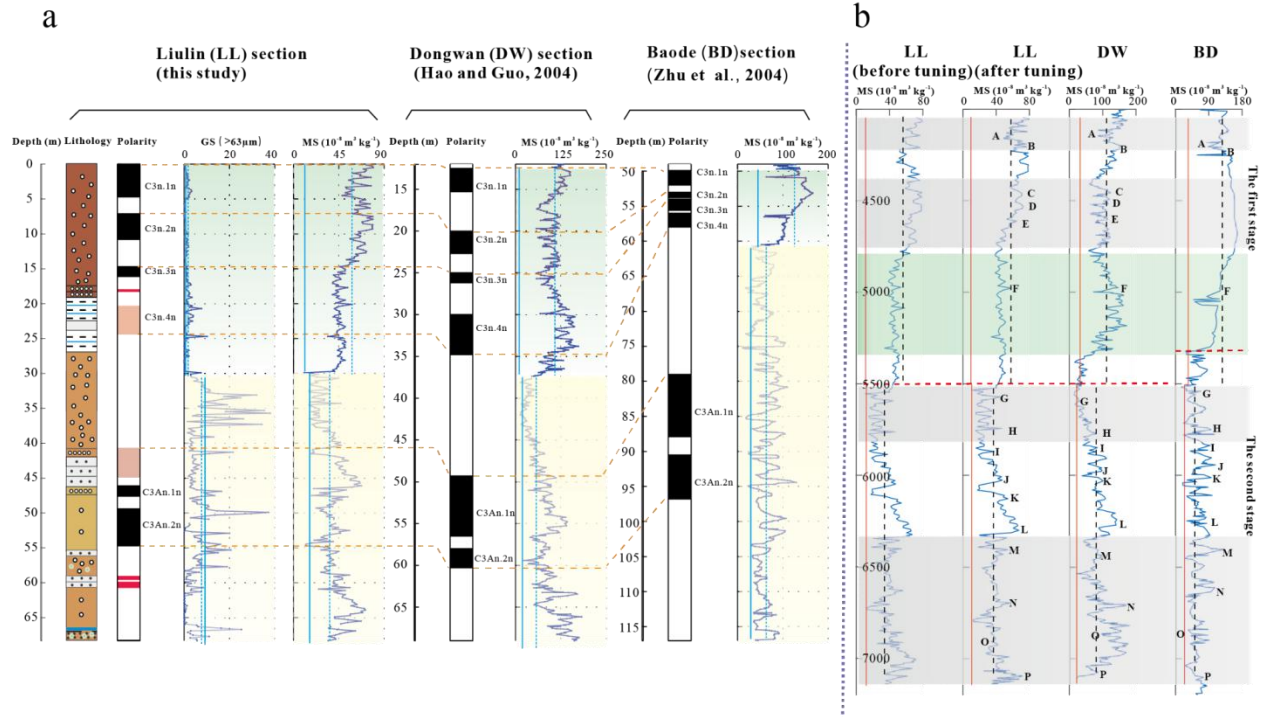
The East Asian monsoon (EAM) system controls precipitation and dust accumulation by the seasonal alternation of inputs of warm moist air from the Indian Ocean and the Pacific Ocean, and dry dust-bearing winds from the high latitudes and high altitudes, which resulted in the creation of the typical sedimentary sequence of the Chinese Loess Plateau (CLP) (Liu, 1985; Kukla and An, 1989; An et al., 1991a, 1991b, 2000; Ding et al., 1992). Heller and Liu (1982) built a robust chronology for the 2.5 Ma loess deposits. The age of underlain eolian red clay was first assigned to the Pliocene at 4 – 5 Ma (Evans et al., 1991; Zheng et al., 1992) and later to the late Miocene at ~7 – 8 Ma (Ding et al., 1998a, Sun et al., 1998a, b; An et al., 2001), the early Miocene at 22 Ma (Guo et al., 2002) and the late Oligocene at 25 Ma (Qiang et al., 2011). Recent magnetostratigraphic studies, however, raised a problem of inconsistency in the reconstructed chronology for the eolian red clay sections in the eastern CLP. For example, a debate exists about the dating of the Jiaxian section where Ding et al. (1998b) considered its deposition started at 5.2 Ma and Qiang et al. (2001) considered it started at 7.2 Ma. Another example of inconsistent age assignments refers to the age of the bottom of the Shilou (SL) section: it was first determined as 11 Ma (Xu et al., 2009), then 5.2 Ma (Anwar et al., 2015) and 8 Ma (Ao et al., 2016). Visual correlation of identified magnetic polarity intervals to the Geomagnetic Polarity Time Scale (GPTS), in the case of the lack of other independent chronostratigraphic constraints, can potentially produce different outcomes, especially when short polarity intervals are considered as geomagnetic subchrons, excursions and tiny wiggles, and even remagnetization (by the groundwater in this study). As a significant improvement in data analysis, the detection of astronomical signals in cyclostratigraphy has provided impressive advancements in stratigraphic correlations, by adjusting the magnetostratigraphic patterns by matching stratigraphic records to the Earth's orbital periodicities typical of the Milankovitch cycles (Anwar et al., 2015; Zhang et al., 2018, 2021a, 2021b, 2022).

## **S2 Stratigraphic correlations from eastern to western CLP**

We compare the LL section to two other classical sections in the eastern and western edges of CLP, in a time interval spanning across the Mio-Pliocene boundary (Supplementary Material Fig. 1). Both Baode (BD) and Dongwan (DW) sections are located close to the mountains (for example, DW is located between Liupan Mts and West Qinling Mts which is close to Tibetan Plateau) as well as LL and SL (Hao and Guo, 2004; Zhu et al., 2008; Xu et al., 2009). These sections might be more affected by the seasonal cyclic variations of the Asian monsoon driven by the tectonic uplift of a series of mountains during the Mio-Pliocene climate transition (Anwar et al., 2015; Zhang et al., 2021b; Zhang et al., 2022).

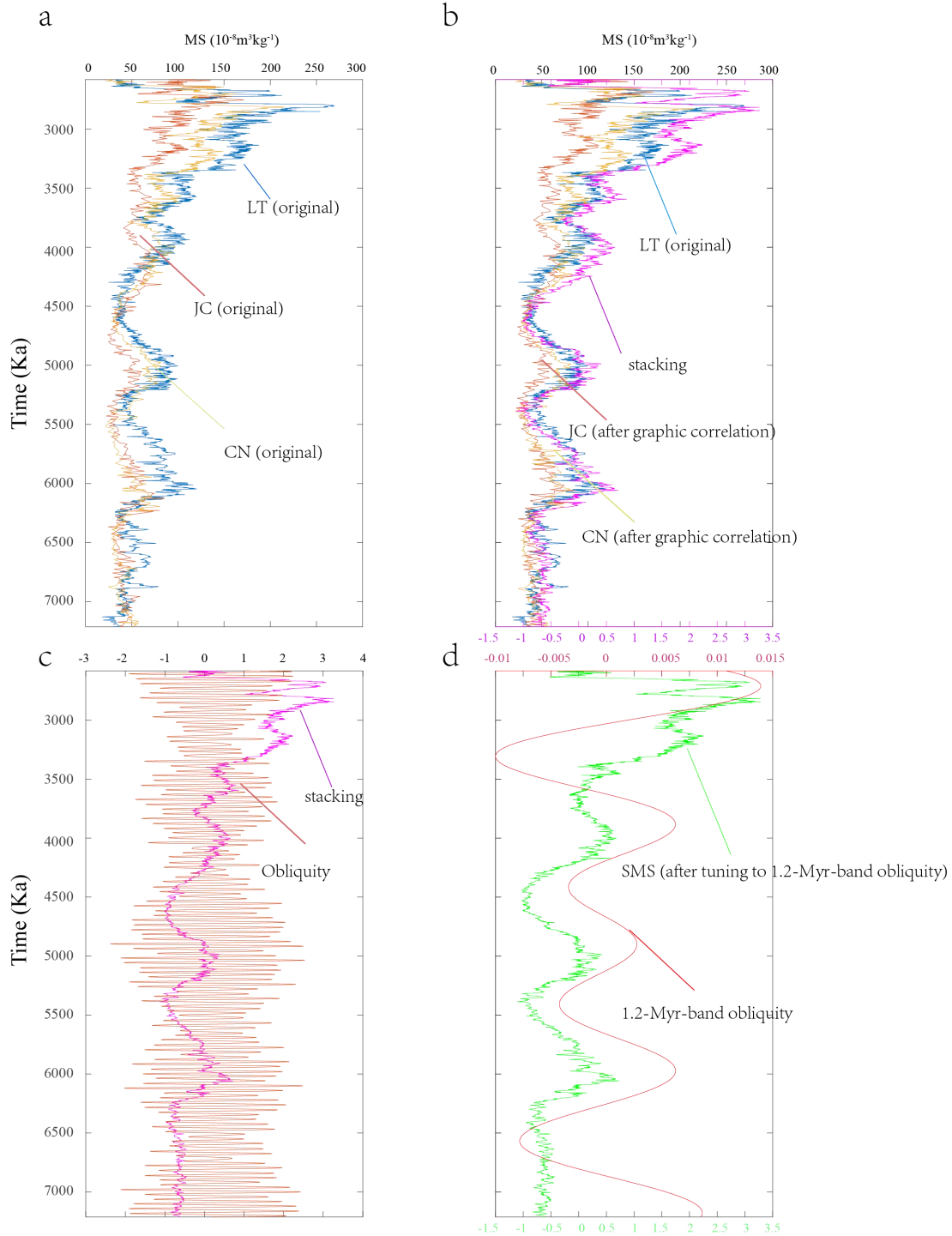
The lower part of the LL section, between 30–68 m, corresponds to the 38–69 m interval in the DW section and to of 60–117 m interval in the BD section, characterized by low MS values (average of  $38 \times 10^{-8} \text{ m}^3/\text{kg}$  for Liulin,  $64 \times 10^{-8} \text{ m}^3/\text{kg}$  for DW,  $59 \times 10^{-8} \text{ m}^3/\text{kg}$  for BD) and wide oscillations (Supplementary Material Fig. 1a). The upper part of the LL section between 0–30 m correlates to the interval of 12–38 m in DW and with an interval of 49–60 m in BD, characterized by distinctly higher MS values (average of  $57 \times 10^{-8} \text{ m}^3/\text{kg}$  for LL,  $123 \times 10^{-8} \text{ m}^3/\text{kg}$  for BD,  $107 \times 10^{-8} \text{ m}^3/\text{kg}$  for DW) and lower amplitude oscillations. The MS variations for each section in the reconstructed time framework are shown in Supplementary Material Fig. 1b. Two stages can be recognized across the LL section: the first stage at depth of 0 – 30 m represents the time interval of 5.5 – 4 Ma and the second stage at the depth of 30 – 68 m represents the time interval of 7 – 5.5 Ma. These data indicate that MS trend reflects a climate transition from lower values with stronger oscillations to higher values with slighter oscillations, while the trend of the coarse fraction ( $>63 \mu\text{m}$ ) content shows a corresponding transition at 30 m (ca. 5.5 Ma), from high values with wide variations in the lower part to low values with limited variations in the upper

part (Supplementary Material Fig. 1). Both MS and GS trends suggest a transition for the Asian atmospheric circulation around the MPB boundary, a shift in the monsoon regime from the strengthening winter and weakening summer to the weakening winter and strengthening summer. This shift is synchronous with the DW section (Hao and Guo, 2004; Li et al., 2008), whereas it appears slightly younger (5.3 Ma) in the BD section (Zhu et al., 2008).

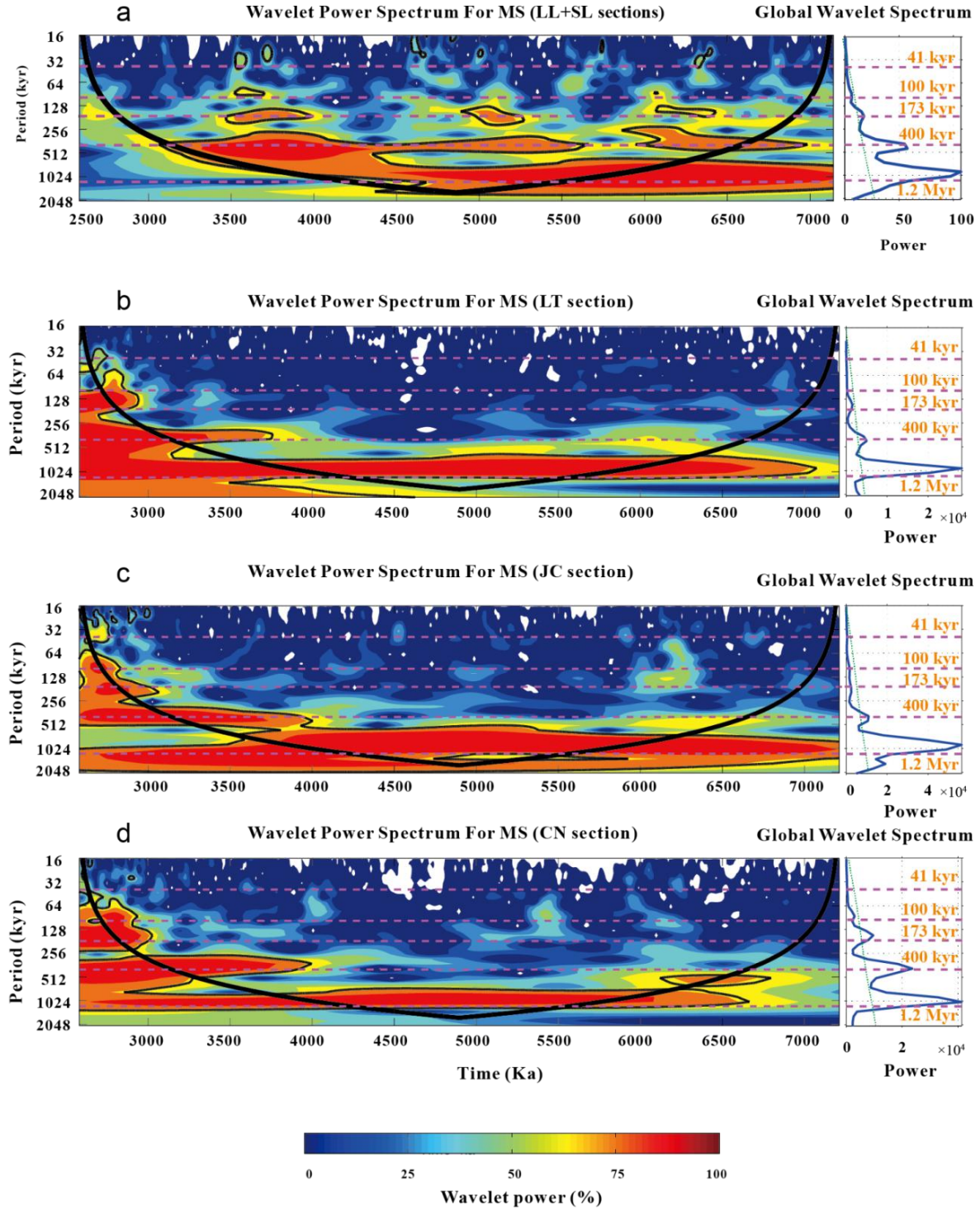


**Supplementary Material Fig. 1.** Comparison of polarity and magnetic susceptibility as a function of depth and age for the red clay sections. (a) LL: Polarity, grain size and MS of the LL red clay section. DW: Polarity and MS of the DW red clay section (Hao and Guo, 2002). BD: Polarity and MS of the BD red clay section (Zhu et al., 2008). The yellow dashed lines correlate the corresponding polarities of each section for mutual comparison. The green and yellow shadings indicate two comparable stages in changing MS for each section. Blue dashed lines represent the average values for each stage and blue solid lines represent the standard deviation. (b) Comparison of MS as a function of age for the red clay sections. LL: MS of the LL red clay section before tuning to eccentricity; MS of the LL red clay section after tuning to eccentricity. DW: MS of the DW red clay section. BD: MS of the BD red clay. The chronology for the DW and BD red clay sequences were obtained from magnetostratigraphy. The gray and white shadings indicate each comparable time interval of the three sections during which consistent variations can be observed. The red dashed lines denote the two stages reflecting different climatic conditions. The black dashed lines represent the average values of each stage and red solid lines represent the standard deviation. A–P shows consistent peaks from MS variations in the three sections during 7–4 Ma.

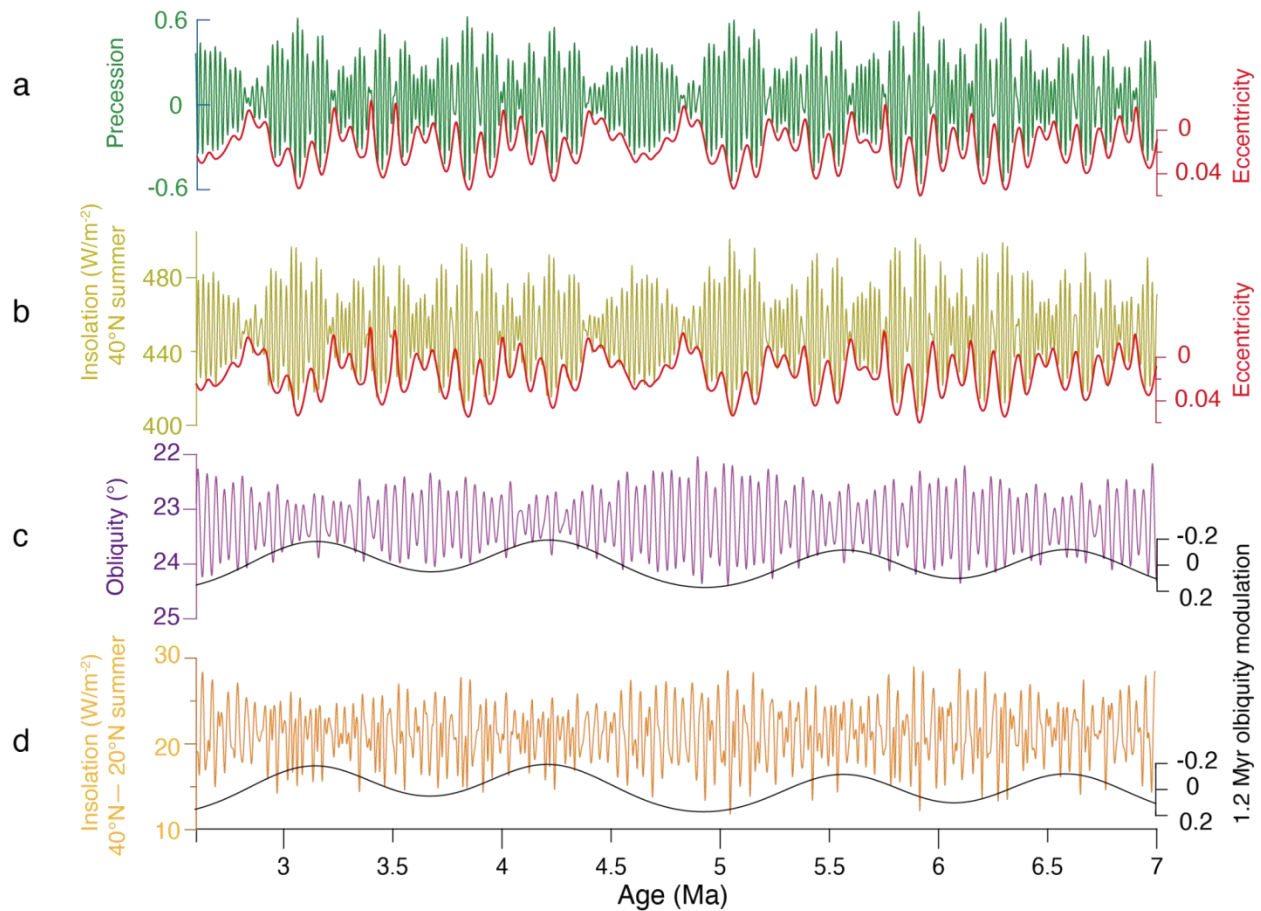




**Supplementary Material Fig. 2.** Illustration of stacking processing of magnetic susceptibility records from the central Chinese Loess Plateau. (a) Original magnetic susceptibility records before processing: blue—LT (Ding et al., 1999), yellow—JC (Ding et al., 2001), brown—CN (Song et al., 2007). (b) Magnetic susceptibility after graphic correlation and stacking. (c) Comparison of the initial stacking data and obliquity solution. (d) Stacked magnetic susceptibility after tuning to the 1.2-Myr-band obliquity.



**Supplementary Material Fig. 3.** Wavelet analysis of magnetic susceptibility records from the central Chinese Loess Plateau. (a) Wavelet spectrum of the Sacked magnetic susceptibility. (b) Wavelet spectrum of magnetic susceptibility from the LT section. (c) Wavelet spectrum of magnetic susceptibility from the JC section. (d) Wavelet spectrum of magnetic susceptibility from the CN section. The purple dashed line marks the orbital period. The thin black contour encloses regions of greater than 95% confidence for a red-noise process with a lag coefficient of 0.8. The thick black contour indicates the cone of influence. The global wavelet spectrum to the right illustrates the mean red noise spectrum, as indicated by the green dashed line. The color bars correspond to wavelet power.



**Supplementary Material Fig. 4.** (a) precession (green line) and eccentricity (red line)(Laskar et al., 2004), (b) boreal summer insolation differences between 40°N and 20°N (yellow line), and eccentricity curves, (c) obliquity (purple line) and 1.2 Myr amplitude modulation curves of obliquity (Laskar et al., 2004), (d) boreal summer insolation differences between 40°N and 20°N (orange line), and amplitude modulation curves of obliquity(black line).

### **S3 - Stacked magnetic susceptibility in the central CLP**

In the past few decades, many studies on successive red clay sections have been conducted through the CLP. Most chronology has been extensively studied and constrained through magnetostratigraphy (Evans, et al., 1991; Ding et al., 1998a,b; Hao and Guo, 2004; Ding et al., 1998a,1998b; Sun et al., 1998a,b; Guo et al., 2002; Qiang et al., 2011). In the main text, we compare the Jingchuan red clay section (Ding et al., 2001) from the middle part of CLP with LL and SL from the eastern CLP. We show clearly the 1.2 Myr obliquity grand cycle observed in these sections. Further, here we integrated the other two well-constrained sections from the heart of CLP, to obtain a composite record of MS signal and Asian monsoon variability. These are Chaona (CN, Song et al., 2007, 2018) and Lingtai (LT, Ding et al., 1998a,1999; Sun et al., 2010), from the central CLP (Supplementary Material Fig. 2). The wavelet power spectrum and global wavelet spectrum (Torrence & Compo, 1998) for the detrended MS records from the above sections, including a stacked MS, documented the amplitude-modulated 1.2 Myr band superimposed on the obliquity and eccentricity cycles for the first time discovery (Supplementary Material Fig. 3).

For stacked magnetic susceptibility (SMS) from LT, CN and JC sections in the central CLP, we started with aligning these records using a graphic correlation technique (Lisiecki and Lisiecki, 2002). Automated correlation algorithms (Lisiecki & Raymo, 2005) provided the first alignment criteria of objective technique to achieve a peak by peak correlation. Each alignment step was also evaluated by stratigraphic features to determine the quality of the matching and to distinguish noise or add tie points. We then chose the age model of one section (herein, LT) as a reference signal to correlate. Each MS record was aligned to the target and then averaged the normalized data at each time level to obtain the initial stacked data. After creating the initial stack, we tuned it to the 1.2-Myr-filtering obliquity as the prominent cycles were visually observed across all these sections (Supplementary Material Fig. 2). The process was iterative, for each result we monitored the spectral presence, if no good orbital cycles showed, we returned to the first step.

Obliquity makes a significant contribution to the seasonal solar radiation (insolation) throughout the year. On a long-term scale of ten thousand years, however, eccentricity constrains insolation (through modulated precession), especially at the mid-high latitudes (Laskar et al., 2004). Supplementary Fig. 4a,b show how the eccentricity modulates boreal summer insolation at 40°N, from 7 to 2.6 Ma. Obliquity-driven variations of summer hydroclimate on the CLP are thought to originate from a meridional gradient of the boreal summer insolation on a ten thousand year timescale as well. The influence of obliquity on the summer insolation is stronger at high latitudes than at low latitudes. Therefore, Supplementary Fig. 4c,d suggest that the 1.2 Myr obliquity modulation can control the monsoon variability through the summer insolation gradients at different latitudes. Here is an example at latitudes between 40 °N and 20 °N. The obliquity modulation enhances the atmospheric circulation and modulates the amount of moisture transported by the southerly summer monsoon from the ocean to land.

## References

- An, Z. (2000). The history and variability of the East Asian paleomonsoon climate. *Quaternary Science Reviews* 19, 171–187.
- An, Z., Kukla, G., Porter, S. C. & Xiao, J. (1991a). Late Quaternary dust flow on the Chinese loess plateau. *Catena* 18, 125–132.
- An, Z., Kukla, G., Porter, S. C. & Xiao, J. (1991b). Magnetic susceptibility evidence of monsoon variation on the Loess Plateau of central China during the last 130,000 years. *Quaternary Research* 36, 29–36.
- An, Z., Kutzbach, J. E., Prell, W. L., & Porter, S. C. (2001). Evolution of Asian monsoons and phased uplift of the Himalaya–Tibetan plateau since Late Miocene times. *nature* 411, 62–66.
- Anwar, T., Kravchinsky, V. A. & Zhang, R. (2015). Magneto - and cyclostratigraphy in the red clay sequence: New age model and paleoclimatic implication for the eastern Chinese Loess Plateau. *Journal of Geophysical Research: Solid Earth* 120, 6758–6770.
- Ao, H., Roberts, A. P., Dekkers, M. J., Liu, X., Rohling, E. J., Shi, Z., An, Z. & Zhao, X. (2016). Late Miocene–Pliocene Asian monsoon intensification linked to Antarctic ice-sheet growth. *Earth and Planetary Science Letters* 444, 75–87.
- Ao, H., Roberts, A. P., Dekkers, M. J., Liu, X., Rohling, E. J., Shi, Z., An, Z., Chang, H., Qiang, X. & Zhao, X. (2018). Reply to Zhang et al.: Late Miocene–Pliocene magnetostratigraphy of the Shilou Red Clay on the eastern Chinese Loess Plateau. *Earth and Planetary Science Letters*, 503, 252–255.
- Ding, Z., Rutter, N., Han, J. & Liu, T. (1992). A coupled environmental system formed at about 2.5 Ma in east-Asia. *Palaeogeography, Palaeoclimatology, Palaeoecology* 94, 223–242.
- Ding, Z., Sun, J., Yang, S. & Liu, T. (1998a). Preliminary magnetostratigraphy of a thick eolian red clay-loess sequence at Lingtai, the Chinese Loess Plateau. *Geophysical Research Letters* 25, 1225–1228.
- Ding, Z., Sun, J., Liu, T., Zhu, R., Yang, S. & Guo, B. (1998b). Wind-blown origin of the Pliocene red clay formation in the central Loess Plateau, China. *Earth and Planetary Science Letters* 161, 135–143.
- Ding, Z., Xiong, S., Sun, J., Yang, S., Gu, Z. & Liu, T. (1999). Pedostratigraphy and paleomagnetism of a ~7.0 Ma eolian loess-red clay sequence at Lingtai, Loess Plateau, north-central China and the implications for paleomonsoon evolution. *Palaeogeography, Palaeoclimatology, Palaeoecology* 152, 49–66.



- Ding, Z., Yang, S., Hou, S., Wang, X., Chen, Z. & Liu, T. (2001). Magnetostratigraphy and sedimentology of the Jingchuan red clay section and correlation of the Tertiary eolian red clay sediments of the Chinese Loess Plateau. *Journal of Geophysical Research: Solid Earth* 106, 6399–6407.
- Evans, M. E., Wang, Y., Rutter, N., Ding, Z. (1991). Preliminary magnetostratigraphy of the red clay underlying the loess sequence at Baoji, China. *Geophysical Research Letters* 18, 1409–1412.
- Guo, Z., Ruddiman, W. F., Hao, Q., Wu, H., Qiao, Y., Zhu, R., Peng, S., Wei, J., Yuan, B. & Liu, T. (2002). Onset of Asian desertification by 22 Myr ago inferred from loess deposits in China. *Nature* 416, 159–163.
- Hao, Q. & Guo, Z. (2004). Magnetostratigraphy of a late Miocene-Pliocene loess-soil sequence in the western Loess Plateau in China. *Geophysical Research Letters* 31.
- Heller, F. & Liu, T. (1982). Magnetostratigraphical dating of loess deposits in China. *Nature* 300, 431–433.
- Kukla, G. & An, Z. (1989). Loess Stratigraphy in Central China. *Palaeogeography Palaeoclimatology Palaeoecology* 72, 203–225.
- Laskar, J., Correia, A.C.M., Gastineau, M., Joutel, F., Levrard, B. & Robutel, P. (2004). Long term evolution and chaotic diffusion of the insolation quantities of Mars. *Icarus*, 170, 343–364.
- Li, F., Rousseau, D. D., Wu, N., Hao, Q. & Pei, Y. (2008). Late Neogene evolution of the East Asian monsoon revealed by terrestrial mollusk record in Western Chinese Loess Plateau: from winter to summer dominated sub-regime. *Earth and Planetary Science Letters* 274, 439–447.
- Lisiecki, L. E. & Lisiecki, P. A. (2002). Application of dynamic programming to the correlation of paleoclimate records. *Paleoceanography*, 17, 1–1.
- Lisiecki, L. E. & Raymo, M. E. (2005). A Pliocene - Pleistocene stack of 57 globally distributed benthic  $\delta^{18}\text{O}$  records. *Paleoceanography*, 20.
- Liu, T. (1985). *Loess and Environment*, pp. 31–67, China Ocean Press, Beijing.
- Ogg, J. G. (2012). Geomagnetic Polarity Time Scale. In F. M. Gradstein, J. G. Ogg, M. D. Schmitz, & G. M. Ogg (Eds.), *The Geologic Time Scale 2012*. Amsterdam: Elsevier, pp. 85–113.
- Qiang, X., An, Z., Song, Y., Chang, H., Sun, Y., Liu, W., Ao, H., Dong, J., Fu, C., Wu, F. & Lu, F. (2011). New eolian red clay sequence on the western Chinese Loess Plateau linked to onset of Asian desertification about 25 Ma ago. *Science China Earth Sciences* 54, 136–144.
- Qiang, X., Li, Z., Powell, C. M. & Zheng, H. (2001). Magnetostratigraphic record of the Late Miocene onset of the East Asian monsoon, and Pliocene uplift of northern Tibet. *Earth and Planetary Science Letters*, 187, 83–93.
- Rutter, N., Ding, Z., Evans, M. E. & Liu, T. (1991). Baoji-type pedostratigraphic section, Loess Plateau, north-central China. *Quaternary Science Reviews* 10, 1–22.
- Song, Y., Fang, X., Torii, M., Ishikawa, N., Li, J. & An, Z. (2007). Late Neogene rock magnetic record of climatic variation from Chinese eolian sediments related to uplift of the Tibetan Plateau. *Journal of Asian Earth Sciences* 30, 324–332.
- Song, Y., Fang, X., Chen, X., Torii, M., Ishikawa, N., Zhang, M., Yang, S. & Chang, H. (2018). Rock magnetic record of late Neogene red clay sediments from the Chinese Loess Plateau and its implications for East Asian monsoon evolution. *Palaeogeography, Palaeoclimatology, Palaeoecology* 510, 109–123.
- Sun, D., An, Z., Shaw, J., Bloemendal, J. & Sun, Y. (1998b). Magnetostratigraphy and palaeoclimatic significance of Late Tertiary aeolian sequences in the Chinese Loess Plateau. *Geophysical Journal International* 134, 207–212.
- Sun, D., John, S., An, Z., Cheng, M. & Yue, L. (1998a). Magnetostratigraphy and paleoclimatic interpretation of a continuous 7.2 Ma Late Cenozoic eolian sediments from the Chinese Loess Plateau. *Geophysical Research Letters* 25, 85–88.
- Sun, Y., An, Z., Clemens, S. C., Bloemendal, J. & Vandenberghe, J. (2010). Seven million years of wind and precipitation variability on the Chinese Loess Plateau. *Earth and Planetary Science Letters* 297, 525–535.
- Torrence, C. & Compo, G.P. (1998). A practical guide to wavelet analysis. *Bulletin of the American Meteorological Society* 79, 61–78.
- Xu, Y., Yue, L., Li, J., Sun, L., Sun, B., Zhang, J., Ma, J. & Wang, J. (2009). An 11-Ma-old red clay sequence on the Eastern Chinese Loess Plateau. *Palaeogeography, Palaeoclimatology, Palaeoecology* 284, 383–391.
- Zhang, R., Kravchinsky, V. A., Anwar, T., Yue, L., Li, J. & Jiao, J. (2018). Comment on "Late Miocene-Pliocene Asian monsoon intensification linked to Antarctic ice-sheet growth"[*Earth Planet. Sci. Lett.* 444 (2016) 75–87]. *Earth and Planetary Science Letters* 503, 248–251.
- Zhang, R., Kravchinsky, V. A., Qin, J., Goguitchaichvili, A. & Li, J. (2021a). One and a Half Million Yearlong Aridity During the Middle Eocene in North-West China Linked to a Global Cooling Episode. *Journal of Geophysical Research: Solid Earth* 126, e2020JB021037.

- Zhang, R., Wei, X., Kravchinsky, V. A., Yue, L., Zheng, Y., Qin, J., Yang, L., Ma, M., Xian, F., Gong, H., Zhang, Y. & Liu, X. (2021b). “Tiny wiggles” in the late Miocene red clay deposits in the north-east of the Tibetan Plateau. *Geophysical Research Letters*, 48, e2021GL093962.
- Zhang, R., Li, X., Xu, Y., Li, J., Sun, L., Yue, L., Pan, F., Xian, F., Wei, X. & Cao, Y. (2022). The 173-kyr obliquity cycle pacing the Asian monsoon in the eastern Chinese Loess Plateau from late Miocene to Pliocene. *Geophysical Research Letters*, 49, e2021GL097008.
- Zheng, H., An, Z. & Shaw, J. (1992). New contributions to Chinese Plio-pleistocene magnetostratigraphy. *Physics of the Earth and Planetary Interiors*, 70, 146–153.
- Zhu, Y., Zhou, L., Mo, D., Kaakinen, A., Zhang, Z. & Fortelius, M. (2008). A new magnetostratigraphic framework for late Neogene Hipparion Red Clay in the eastern Loess Plateau of China. *Palaeogeography, Palaeoclimatology, Palaeoecology* 268, 47–57.